Lagrangian Drifter Dispersion in the Surf Zone: Directionally Spread, Normally Incident Waves

Matthew Spydell and Falk Feddersen

Integrative Oceanography Division, Scripps Institution of Oceanography, La Jolla, California

ABSTRACT

Lagrangian drifter statistics in a surf zone wave and circulation model are examined and compared to single- and two-particle dispersion statistics observed on an alongshore uniform natural beach with small, normally incident, directionally spread waves. Drifter trajectories are modeled with a time-dependent Boussinesq wave model that resolves individual waves and parameterizes wave breaking. The model reproduces the cross-shore variation in wave statistics observed at three cross-shore locations. In addition, observed and modeled Eulerian binned (means and standard deviations) drifter velocities agree. Modeled surf zone Lagrangian statistics are similar to those observed. The single-particle (absolute) dispersion statistics are well predicted, including nondimensionalized displacement probability density functions (PDFs) and the growth of displacement variance with time. The modeled relative dispersion and scale-dependent diffusivity is consistent with the observed and indicates the presence of a 2D turbulent flow field. The model dispersion is due to the rotational components of the modeled velocity field, indicating the importance of vorticity in driving surf zone dispersion. Modeled irrotational velocities have little dispersive capacity. Surf zone vorticity is generated by finite crest-length wave breaking that results, on the alongshore uniform bathymetry, from a directionally spread wave field. The generated vorticity then cascades to other length scales as in 2D turbulence. Increasing the wave directional spread results in increased surf zone vorticity variability and surf zone dispersion. Eulerian and Lagrangian analysis of the flow indicate that the surf zone is 2D turbulent-like with an enstrophy cascade for length scales between approximately 5 and 10 m and an inverse-energy cascade for scales of 20 to 100 m. The vorticity injection length scale (the transition between enstrophy and inverse-energy cascade) is a function of the wave directional spread.

1. Introduction

Terrestrial runoff dominates urban pollutant loading rates (Schiff et al. 2000). Often draining directly onto the shoreline, runoff pollution degrades surf zone water quality, leading to beach closures (e.g., Boehm et al. 2002). Runoff increases the health risks (e.g., diarrhea and upper respiratory illness) to ocean bathers (Haile et al. 1999) and contains both human viruses (Jiang and Chu 2004) and elevated levels of fecal indicator bacteria (Reeves et al. 2004). Surf zone mixing processes disperse and dilute such pollution. The surf zone and nearshore region are a vital habitat to ecologically and economically important species of marine fish (e.g., Romer and McLachlan 1986) and invertebrates (e.g., Lewin 1979). The same surf zone dispersal processes likely affect nutrient availability, primary productivity, and larval dispersal (e.g., Talbot and Bate 1987; Denny and Shibata 1989). Understanding surf zone Lagrangian dispersion processes is important to predicting the fate (transport, dispersal, and dilution) of surf zone tracers, whether pollution, bacteria, larvae, or nutrients.

Previous surf zone dispersion studies have generally tracked fluorescent dye (Harris et al. 1963; Inman et al. 1971; Grant et al. 2005; Clarke et al. 2007), resulting in estimated "eddy" diffusivity magnitudes that vary considerably. These studies have difficulties in detailed dye tracking and are based on single realizations. Surf zone Lagrangian drifters also are used to study dispersion. Johnson and Pattiaratchi (2004) used the spreading rate of multiple drifters to estimate scale-dependent relative diffusivities in the surf zone on a beach with a dominant rip current circulation feature. For approximately 10–50-m separations, relative diffusivities between 1.3 and 3.9 $m^2 s^{-1}$ were reported.

Corresponding author address: M. Spydell, SIO, 9500 Gilman Dr., La Jolla, CA 92093–0209.
E-mail: mspydell@ucsd.edu

Two days of surf zone drifter dispersion observations on an alongshore uniform beach were reported by Spydell et al. (2007). The first day had small normally incident waves with weak mean currents; the second had large obliquely incident waves driving a strong alongshore current. Absolute and relative Lagrangian statistics were presented for both days. On the first day, the observed drifter dispersion had properties similar to a two-dimensional (2D) turbulent fluid, and the scale-dependent relative diffusivity suggested the presence of a surf zone eddy (vorticity) field with a range of length scales spanning 5–50 m (Spydell et al. 2007). The lack of any mean currents precludes sheared currents as the source of this eddy field; the presence of finite crest length breaking waves was hypothesized to generate the vertical vorticity (Peregrine 1998). This vorticity could then cascade to other length scales analogous to the vorticity dynamics of 2D turbulence. On an alongshore uniform beach, finite breaking crest length is the result of nonzero wave directional spread σ_θ (e.g., Kuik et al. 1988), that is, incoming waves with a variety of angles.

Accurately modeling and diagnosing surf zone dispersion requires resolving dynamics on a wide range of time scales from surface gravity waves (a few seconds) to very low-frequency vortical motions (1000 s) and length scales from a few meters to many multiple surf zone widths (1000 m). In addition, representing the effects of finite crest length wave breaking is hypothesized to be important. Time-dependent Boussinesq wave models (e.g., Nwogu 1993; Wei et al. 1995) that simulate wave breaking with an eddy viscosity term in the momentum equations (e.g., Chen et al. 1999; Kennedy et al. 2000) associated with the front face of steep (breaking) waves fit these requirements. These types of Boussinesq models reproduce observed wave height variation across the surf zone in the laboratory (Kennedy et al. 2000) and field (Chen et al. 2003). In addition to representing the 2D (horizontal) nature of shoaling and breaking waves (Chen et al. 2000), Boussinesq model simulations with directionally spread waves give rise to a rich surf zone eddy field with vorticity variability over a range of scales (Chen et al. 2003; Johnson and Pattiaratchi 2006).

Here, the question of whether surf zone vorticity and the resulting Lagrangian dispersion are consistent with a ''2D turbulent'' fluid is examined with Eulerian and Lagrangian statistics. In forced 2D turbulence, energy is injected at a particular length scale. The resulting turbulent eddies then cascade to other length scales following 2D vorticity dynamics, resulting in two classifiable regimes: the inverse-energy and enstrophy cascade regions. In the inverse-energy cascade of 2D (and also in inertial subrange of 3D) turbulence (i.e., spatial scales larger than the turbulent injection scale), the Eulerian signature is an $E \sim K^{-5/3}$ velocity wavenumber spectrum, whereas the Lagrangian signatures relate to particle separation statistics. Specifically, the variance of particle separations depends on the cube of time $D^2 \sim t^3$, the probability density function (PDF) of separations is non-Gaussian $[P(r) \sim \exp(-|r|^{2/3})]$, and the relative diffusivity depends on the separation $\kappa \sim r^{4/3}$. These scalings are collectively considered Richardson's laws, which were first obtained empirically for atmospheric data (Richardson 1926). The theoretical basis of these scalings (excluding the PDF shape) derives from dimensional arguments (Obukhov 1941a,b; Batchelor 1950). These laws have subsequently been observed in direct numerical simulation (DNS) of 2D (Boffetta and Sokolov 2002b) and 3D (Boffetta and Sokolov 2002a) turbulence and in laboratory experiments of 2D turbulence (Jullien et al. 1999). Furthermore, some oceanic observations are consistent with Richardson's laws (e.g., Stommel 1949; Okubo 1971). In the enstrophy cascade of 2D turbulence (i.e., spatial scales smaller than the turbulent injection scale), the energy spectrum is given by $E(k) \sim k^{-3}$, with separation variance growing exponentially $[D^2 \sim \exp(t)]$ and the relative diffusivity strongly scale-dependent ($\kappa \sim D^2$). These Lagrangian enstrophy cascade laws were originally motivated by atmospheric data (Lin 1972) and later observed in laboratory experiments of 2D turbulence (Jullien 2003).

Here the Spydell et al. (2007) day 1 surf zone drifter observations (section 2) are simulated with a Boussinesq model, described in section 3. Lagrangian single- and two-particle statistics are described in section 4. Model–data comparison of the Eulerian wave and current statistics give good agreement (section 5), indicating that the surf zone processes are reasonably represented by the model. Lagrangian absolute and relative dispersion model–data comparison is reported in section 6. Both absolute and relative dispersion statistics compare well, although the magnitude of the observed relative dispersion is larger and scales more slowly with time than the modeled relative dispersion. Both enstrophy and inverse-energy cascades are inferred from the modeled Lagrangian statistics.

The Boussinesq model is used to diagnose the underlying processes leading to the modeled dispersion. Model velocity fields are decomposed into irrotational and rotational components and drifters are advected within each velocity field (section 7). At times > 30 s, (absolute and relative) dispersion is dominated by rotational velocities, indicating the importance of vorticity even on an alongshore uniform bathymetry with weak alongshore currents. The vorticity generation mechanism is the nonzero curl of the force imparted by the

Boussinesq model wave breaking formulation. This mechanism is identical to the alongshore gradients in breaking wave dissipation discussed in Peregrine (1998) and requires a directionally spread wave field to create finite breaking crest lengths. Boussinesq model simulations with varying incoming wave directional spread σ_{θ_0} are used to investigate the relationship among σ_{θ_0}, the fluctuating vorticity field, and the resulting surf zone drifter dispersion (section 8). Eulerian analysis of the model data at various σ_{θ_0} reveals regimes of both enstrophy and inverse-energy cascades, with the length scale separating the two regimes depending upon σ_{θ_0}; that is, the length scale of vorticity injection is σ_{θ_0} dependent. This vorticity then freely evolves and cascades to other length scales in a 2D turbulence-like fashion. The results are summarized in section 9.

2. Observations

Observations of surf zone drifter dispersion were acquired on 3 November 2004 at Torrey Pines beach in San Diego, California with small, normally incident, directionally spread waves and weak mean currents. These observations are reported in detail in Spydell et al. (2007) and are briefly described here. The cross- and alongshore coordinates are x and y, with $x = 0$ m the mean shoreline and x increasing negatively offshore. Locally, the bathymetry was nearly uniform alongshore. The bathymetry alongshore uniformity statistic (Ruessink et al. 2001) is $\chi^2 = 0.0036$ in the inner surf zone region, an order of magnitude smaller than that found to create alongshore nonuniform circulation (Ruessink et al. 2001; Feddersen and Guza 2003). Three Sontek Triton acoustic Doppler velocimeters (ADVs), sampling at 2 Hz, were deployed on a cross-shore transect with sensing volumes 0.8 m above the bed and were used to estimate wave statistics such as significant wave height H_s, mean wave angle $\bar{\theta}$, and wave directional spread σ_θ (see appendix).

Drifter deployments were conducted over 6 h with roughly stationary wave, current, and tide conditions (Spydell et al. 2007). There were nine separate releases of nine drifters on a cross-shore transect. A total of 77 drifter trajectories, approximately 1000 s long, passed quality control. The freely floating, impact-resistant, GPS-tracked surf zone drifters are 0.5-m tall cylinders with most of their volume below the water line. A horizontal disc at the bottom of the body tube dampens vertical motions in the waves, allowing broken waves to pass over the drifter without pushing or "surfing" it ashore. Drifter GPS positions are internally recorded at 1 Hz, with an absolute position error of about ± 4 m (George and Largier 1996). Postprocessing using carrier

phase information reduces the absolute error to ± 1 m (Doutt et al. 1998). Technical descriptions of the drifters and their response are found in Schmidt et al. (2003).

3. The Boussinesq wave and current model

A time-dependent Boussinesq wave model similar to FUNWAVE (e.g., Chen et al. 1999), which resolves individual waves and parameterizes wave breaking, is used to numerically simulate velocities and sea surface height in the surf zone. The Boussinesq model equations are similar to the nonlinear shallow water equations but include higher-order dispersive terms (and in some derivations higher-order nonlinear terms). Here the equations of Nwogu (1993) are implemented. The equation for mass (or volume) conservation is

$$\frac{\partial \eta}{\partial t} + \nabla \cdot [(h + \eta)\mathbf{u}] + \nabla \cdot \mathbf{M}_d = 0, \tag{1}$$

where η is the instantaneous free surface elevation, t is time, h is the still water depth, and $\mathbf{u}$ is the instantaneous horizontal velocity at the reference depth $z_r = -0.531$ h, where $z = 0$ at the still water surface. The dispersive term $\mathbf{M}_d$ in (1) is

$$\mathbf{M}_d = \left(\frac{z_r^2}{2} - \frac{h^2}{6}\right) h\nabla(\nabla\mathbf{u}) + (z_r + h/2)h\nabla[\nabla \cdot (h\mathbf{u})]. \tag{2}$$

The momentum equation is

$$\frac{\partial \mathbf{u}}{\partial t} + \mathbf{u} \cdot \nabla\mathbf{u} = -g\nabla\eta + \mathbf{F}_d + \mathbf{F}_{\mathrm{br}} - \frac{\tau_b}{(\eta + h)} - \nu_{\mathrm{bi}}\nabla^4\mathbf{u}, \tag{3}$$

where g is gravity, $\mathbf{F}_d$ are the higher-order dispersive terms, $\mathbf{F}_{\mathrm{br}}$ are the breaking terms, τ_b is the instantaneous bottom stress, and ν_{bi} is the hyperviscosity for the biharmonic friction ($\nabla^4\mathbf{u}$) term. The dispersive terms are (Nwogu 1993)

$$\mathbf{F}_d = - \left\{\frac{z_r^2}{2}\nabla(\nabla \cdot \mathbf{u}_t) + z_r\nabla[\nabla \cdot (h\mathbf{u}_t)]\right\},$$

and the bottom stress is parameterized with a quadratic drag law

$$\tau_b = c_d|\mathbf{u}|\mathbf{u},$$

with the nondimensional drag coefficient c_d.

Following Kennedy et al. (2000), the effect of wave breaking on the momentum equations is parameterized as a Newtonian damping where

$$\mathbf{F}_{\mathrm{br}} = (h + \eta)^{-1}\nabla \cdot [\nu_{\mathrm{br}}(h + \eta)\nabla\mathbf{u}],$$
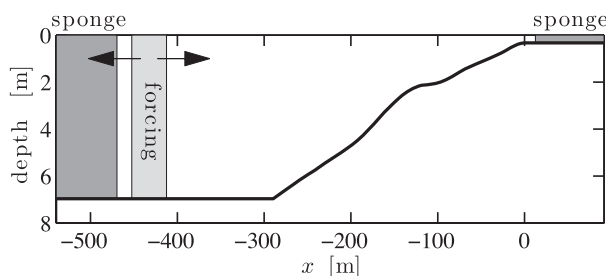
FIG. 1. Schematic of the model bathymetry vs cross-shore coordinate x. The dark shaded regions indicate the sponge layer locations and the light shading indicates the wave generation region, which radiates waves onshore and offshore (into the sponge layer) as indicated by the arrows.

where ν_{br} is the eddy viscosity associated with the breaking waves.[1] The breaking eddy viscosity is given by

$$\nu_{\mathrm{br}} = B\delta^2(h + \eta)\frac{\partial\eta}{\partial t}, \qquad (4)$$

where δ is a constant and B is a function of η_t and varies between 0 and 1. When η_t is sufficiently large (i.e., the front face of a steep breaking wave), B becomes nonzero. The Kennedy et al. (2000) expression for B is used here. The wave breaking parameter choices are similar to the ones used by Kennedy et al. (2000) to model laboratory breaking waves and by Chen et al. (2003) for modeling laboratory and field wave heights and alongshore currents. The model results are not overly sensitive to these choices.

The model equations [e.g., (1) and (3)] are second-order spatially discretized on a C grid (Harlow and Welch 1965) and time integrated with a third-order Adams–Bashforth (Durran 1991) scheme. The model extent is 482 m in the cross shore dimension, excluding sponge layers (see Fig. 1), and 2000 m in the alongshore. The alongshore boundary conditions are periodic. The cross-shore and alongshore grid spacings are 1 and 2 m, respectively. The model time step is $\Delta t = 0.01$ s. The bathymetry is alongshore uniform and equal to the alongshore mean of the observed bathymetry (Fig. 1). The location of $x = 0$ m is where the observed mean depth becomes $h = 0$ m (i.e., the mean shoreline). Onshore of $x \approx 0$ m, the model bathymetry becomes flat, with $h = 0.2$ m for an additional 92 m. The last 80 m of the flat region is a sponge layer (Fig. 1) that absorbs any wave energy not yet dissipated by wave breaking. At $x = -290$ m, the (observed and model) depth is $h = 7$ m; farther offshore the model depth is flat. At the offshore

end of the model domain, a second 70-m-long sponge layer (Fig. 1) absorbs outgoing wave energy so that it is not reflected.

Random directionally spread waves are generated by oscillating the sea surface η on an offshore source strip Wei et al. (1999), with the 40-m cross-shore width located at $x = -445$ m in $h = 7$ m depth (light shaded region in Fig. 14). Within this strip, η is forced at 701 individual frequencies from 0.0626 to 0.2 Hz with 21 directional components at each frequency. The 701 frequencies and 21 directions were sufficient that the source standing wave problem discussed in Johnson and Pattiaratchi (2006) did not occur here. The angles (or alongshore wavenumbers) for the directional components are chosen to satisfy alongshore periodicity (Wei et al. 1999). The directional magnitudes are Gaussian so that at each frequency the mean wave angle is zero and the wave spread is constant with frequency. The forcing amplitudes (and thus the incident spectrum) are set with random phases so that the model reproduces the wave spectra, the mean wave angle $\bar{\theta}$, and the directional spread σ_{θ} (see appendix) at the most offshore instrument. At the peak frequency $f_p = 0.08$ Hz and $kh = 0.45$ (where k is the wavenumber), and at the highest forced frequency $f = 0.2$ Hz and $kh = 1.3$, which is within the valid Nwogu (1993) Boussinesq equation kh range for wave phase speed (Gobbi et al. 2000). At the wavemaker $H_s/h = 0.07$; thus, wavemaker nonlinearities are small.

The nondimensional drag coefficient $c_d = 2 \times 10^{-3}$ is consistent with surf zone alongshore momentum balances (e.g., Feddersen et al. 1998) and with previous alongshore current studies using Boussinesq models (Chen et al. 2003). Biharmonic friction is necessary to dampen nonlinear aliasing instabilities in the model and the hyperviscosity is set to $\nu_{\mathrm{bi}} = 0.3$ m^4 s^{-1}. Biharmonic friction has negligible influence on scales larger than 10 m (e.g., with $L = 10$ m, the biharmonic Reynolds number $UL^3/\nu_{\mathrm{bi}} = 6000$). As an example, a snapshot of instantaneous η and vorticity is shown in Fig. 2. Note that the directionally spread wave field results in wave crests with finite length (Fig. 2a).

After the model reached a statistically steady state (1000 s into the model run), 2000 model surf zone drifters were released uniformly distributed within $-240 < x < 0$ m and advected by the model's horizontal velocities (at the reference depth $z_r = -0.531h$). Similar to the real drifters (Schmidt et al. 2003), the model drifters do not surf onshore at the passage of a bore. Furthermore, model drifters do not feel bore-induced turbulence and thus disperse differently than a tracer (Feddersen 2007). The model drifters were tracked for approximately 2000 s with positions output every 0.5 s.

---

[1] The Newtonian damping form used here differs slightly from that in Kennedy et al. (2000), where $\mathbf{F}_{\mathrm{br}} = (1/2)(h + \eta)^{-1}\boldsymbol{\nabla} \cdot [\nu_{\mathrm{br}}(h + \eta)(\boldsymbol{\nabla}_u + \boldsymbol{\nabla}_u)^{\mathrm{T}}]$ was used.

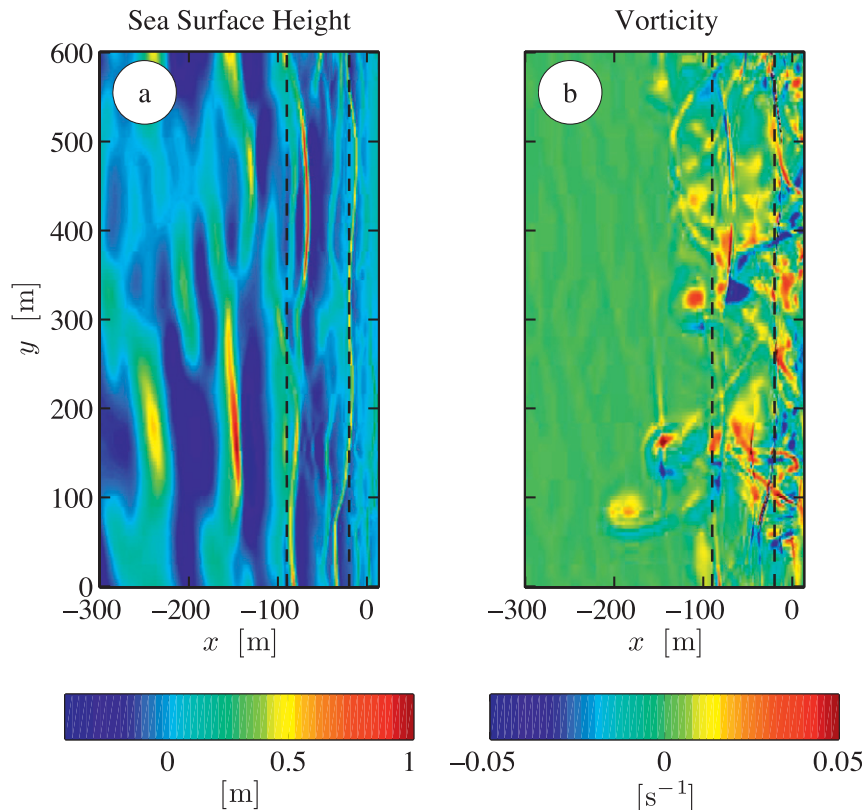Sea Surface Height   Vorticity

FIG. 2. Model output snapshot, 2200-s postmodel spinup, of (a) the sea surface elevation η and (b) the vorticity for an incoming wave spread of $\sigma_{\theta_0} = 14°$. The shoreline is located near $x = 0$ m. Notice significant vorticity mostly onshore of $x = -150$ m. The vertical dashed lines indicate the inner surf zone region ($-90 < x < -20$ m) where Lagrangian drifter analysis is performed.

When model drifters advect onshore of $x = 0$ m, the drifter track is omitted from the dispersion calculations. Note that aside from setting the wavemaker forcing amplitudes to reproduce the most offshore ADV wave spectra, no other tuning of model coefficients has been performed to optimize the model fit to data.

4. Lagrangian drifter statistics background

The notation, theory, and techniques used to calculate the single- and two-particle Lagrangian statistics from drifter trajectories, whether observed or modeled, are introduced in this section. Note that the adjectives "single-particle" and "absolute" are synonymous when describing dispersion or diffusivities, as are the adjectives "two-particle" and "relative."

a. Single-particle statistics

The position of the ith particle at time t is

$$\mathbf{X}^{(i)}(t) = \mathbf{X}_0^{(i)} + \int_0^t \mathbf{v}^{(i)}(\tau)\, d\tau,$$

where $\mathbf{v}^{(i)}(\tau)$ is the Lagrangian particle velocity along its trajectory and $\mathbf{X}_0^{(i)} = \mathbf{X}^{(i)}(t = 0)$ is the initial particle location. The particle displacement from its original position is then

$$\mathbf{a}^{(i)}(t|\mathbf{X}) = \mathbf{X}^{(i)}(t) - \mathbf{X}_0^{(i)} = \int_0^t \mathbf{v}^{(i)}(\tau)\, d\tau.$$

The notation $t|\mathbf{X}$ is used to indicate that the particle is at (in practice in the bin) $\mathbf{X}$ at time t. This dependency on position is necessary because Lagrangian statistics depend on position in inhomogeneous flows. Trajectories are "binned" by final particle position when calculating absolute dispersion in inhomogeneous flows (Davis 1991). The mean displacement after time t is

$$\bar{\mathbf{a}}(t|\mathbf{X}) = \langle \mathbf{a}^{(i)}(t|\mathbf{X}) \rangle, \qquad (5)$$

with the expectation $\langle \cdot \rangle$ operating over all length t particle displacements that end in the bin $\mathbf{X}$. Note that this expectation, as long as the particle never leaves the bin $\mathbf{X}$, can be constructed for a single particle (not just an

ensemble of many) because the time $t = 0$ is arbitrary. Thus, for a 5-s particle track there are five nonoverlapping (but not necessarily independent) 1-s displacements. The mean displacement (5) is also the integral of the mean Lagrangian velocity

$$\bar{\mathbf{a}}(t|\mathbf{X}) = \int_0^t \bar{\mathbf{v}}(\tau|\mathbf{X})d\tau,$$

which naturally leads to the displacement anomaly

$$\mathbf{a}'(t|\mathbf{X}) = \mathbf{a}(t|\mathbf{X}) - \bar{\mathbf{a}}(t|\mathbf{X}) = \int_0^t \mathbf{v}'(\tau|\mathbf{X})d\tau, \qquad (6)$$

where $\mathbf{v}'(\tau|\mathbf{X})$ is the anomalous Lagrangian velocities. The superscript (i) denoting particle number on $\mathbf{a}$ and $\mathbf{a}'$ is dropped because it is no longer relevant to single-particle statistics.

Quantities that depend on the "absolute" displacement $\mathbf{a}'$ will be designated with a superscript (a). The PDF of displacement anomalies is $P^{(a)}(\mathbf{X}, a'_x, a'_y, t)$ and the $P^{(a)}$ spreading rate is the absolute diffusivity $\kappa^{(a)}(\mathbf{X}, t)$. In homogeneous turbulent fluids, $P^{(a)}$ is expected to be Gaussian. In fluids with homogeneous turbulent statistics, the absolute dispersion tensor is defined as

$$[D_{ij}^{(a)}(t)]^2 = \langle a'_i(t)a'_j(t)\rangle,$$

and the absolute diffusivity is (Taylor 1921)

$$\kappa_{ij}^{(a)} = \frac{1}{2}\frac{d}{dt}[D_{ij}^{(a)}(t)]^2.$$

However, the surf zone and nearshore (and many other oceanographic regions) do not have homogeneous turbulent velocity statistics. For example, the region just seaward of the surf zone was observed to have smaller diffusivities than within the surf zone (Spydell et al. 2007).

The absolute dispersion concepts introduced by Taylor (1921) have been extended by Davis (1987, 1991) to flows with inhomogeneous statistics such as the surf zone. In these situations, the spatially variable absolute diffusivity tensor is (Davis 1991)

$$\kappa_{ij}^{(a)}(\mathbf{X},t) = \int_0^t C_{ij}(\mathbf{X}, \tau)\, d\tau, \qquad (7)$$

where $C_{ij}(\mathbf{X}, \tau)$ is the Lagrangian velocity auto-covariance function defined as

$$C_{ij}(\mathbf{X},\tau) = \langle v'_i(t|\mathbf{X})v'_j(-\tau + t|\mathbf{X})\rangle.$$

Thus, $C_{ij}(\mathbf{X}, \tau)$ is the τ-separated autocorrelation of particle velocities binned according to the final location $\mathbf{X}$ of the particles. The absolute dispersion is then

$$D_{ij}^{(a)}(\mathbf{X},t) = \left[2\int_0^t \kappa_{ij}^{(a)}(\mathbf{X},\tau)d\tau\right]^{1/2}$$

and is a measure of the size of the ensemble averaged patch.

Single-particle dispersion is typically divided into two time regimes, the "ballistic" and "Brownian" regimes, which essentially assume a monotonically decaying and integrable $C_{ij}(\tau)$. For times less than the Lagrangian decorrelation time scale, called the ballistic regime,

$$[D_{ij}^{(a)}(t)]^2 \sim 2E_{ij}t^2$$
$$\text{for } t < \mathrm{T}_{L,ij}, \qquad (8)$$
$$\kappa_{ij}^{(a)}(t) \sim 2E_{ij}t,$$

where

$$E_{ij} = \frac{1}{2}C_{ij}(0) = \frac{1}{2}\langle v'_i(0)v'_j(0)\rangle,$$

is the Lagrangian energy. In the Brownian regime, many times larger than the Lagrangian time scale,

$$[D_{ij}^{(a)}(t)]^2 \sim 2\kappa_{ij}^{(a)\infty}t$$
$$\text{for } t > \mathrm{T}_{L,ij}. \qquad (9)$$
$$\kappa_{ij}^{(a)\infty} \sim 2E_{ij}T_{L,ij}$$

Thus, $[D^{(a)}]^2$ initially scales like t^2 and subsequently like t once the Lagrangian velocities are uncorrelated. Note that all quantities E_{ij}, $T_{L,ij}$, and $\kappa^{(a)\infty}$ in the above asymptotic formulas depend on position $\mathbf{X}$.

The absolute diffusivity $\kappa^{(a)}$ parameterizes eddy fluxes for the evolution of the ensemble-averaged tracer $\bar{c}(\mathbf{x}, t)$. In an inhomogeneous flow field, $\bar{c}(\mathbf{x}, t)$ is governed by (Davis 1987)

$$\frac{\partial}{\partial t}\bar{c} + \bar{\mathbf{u}}\cdot\nabla\bar{c} = \nabla\cdot\left[\int_0^\tau \frac{\partial\kappa^{(a)}(\mathbf{x},t')}{\partial t'}\cdot\nabla\bar{c}(t-t')dt'\right], \quad (10)$$

where $\bar{\mathbf{u}}$ is the mean fluid velocity and $\kappa^{(a)}$ is the particle-derived absolute diffusivity from (7). For times longer than the Lagrangian decorrelation time T_L and without mean flow, tracer evolution takes the familiar form

$$\frac{\partial}{\partial t}\bar{c} = \nabla\cdot[\kappa^{(a)\infty}(\mathbf{x})\cdot\nabla\bar{c}]. \qquad (11)$$

One of the purposes of single-particle statistics is to estimate the diffusivities in (10) and (11).

b. Two-particle statistics

The separation between two particles is

$$\mathbf{R}^{(ij)}(t) = \mathbf{X}^{(i)}(t) - \mathbf{X}^{(j)}(t),$$

where $\mathbf{X}^{(i)}(t)$ and $\mathbf{X}^{(j)}(t)$ are the locations of two distinct particles. The amount the two particles have separated from their original separation $\mathbf{R}^{(ij)}(t = 0) = \mathbf{R}_0^{(ij)}$ is

$$\mathbf{r}^{(ij)}(t) = \mathbf{R}^{(ij)}(t) - \mathbf{R}_0^{(ij)},$$

and the separation anomaly is

$$\mathbf{r}'^{(ij)}(t|\mathbf{X}_m, \mathbf{R}_0) = \mathbf{r}^{(ij)}(t) - \bar{\mathbf{r}}(t|\mathbf{X}_m, \mathbf{R}_0),$$

where $\bar{\mathbf{r}}(t|\mathbf{X}_m, \mathbf{R}_0) = \langle \mathbf{r}^{(ij)}(t|\mathbf{X}_m, \mathbf{R}_0) \rangle$ and ensemble averages are taken over all particle pairs with the same initial separation $\mathbf{R}_0$ and same initial location of the pair $\mathbf{X}_m$—the pair's initial midpoint. Thus, unlike the notation used for single-particle statistics, $t|\mathbf{X}_m, \mathbf{R}_0$ for two particles means that at $t = 0$ the midpoint of the particles is $\mathbf{X}_m$ and the initial separation is $\mathbf{R}_0$. The probability density function of particle separation anomalies is denoted by $P^{(r)}(\mathbf{X}_m, \mathbf{R}_0, \mathbf{r}', t)$, where the superscript r denotes "relative."

The "width" of this PDF is given by the relative dispersion

$$D_{ij}^{(r)}(\mathbf{X}_m, \mathbf{R}_0, t) = [\langle r_i'(t|\mathbf{X}_m, \mathbf{R}_0) r_j'(\mathbf{X}_m, \mathbf{R}_0) \rangle]^{1/2},$$

which indicates how far the particles have separated from their initial separation. The relative diffusivity $\kappa_{ij}^{(r)}$ is the rate two particles separate and is defined as

$$\kappa_{ij}^{(r)}(\mathbf{X}_m, \mathbf{R}_0, t) = \frac{1}{2} \frac{d}{dt} [D_{ij}^{(r)}(\mathbf{X}_m, \mathbf{R}_0, t)]^2.$$

In 2D homogeneous isotropic turbulence, the statistics of particle separations are known. In the inverse-energy cascade range (the inertial subrange; i.e., for length scales larger than the injection scale of the turbulence), the velocity wavenumber spectrum scales as $E(k) \sim k^{-5/3}$ and the relative dispersion scalings are

$$P^{(r)}(r') \sim \exp(-|r'|^{2/3}), \tag{12a}$$

$$[D^{(r)}(t)]^2 \sim t^3, \tag{12b}$$

$$\kappa^{(r)} \sim [D^{(r)}]^{4/3}. \tag{12c}$$

These scalings (12) are called Richardson's laws and have been observed in simulations of isotropic inertial subrange 3D turbulence (Boffetta and Sokolov 2002a), simulations of 2D turbulence (Boffetta and Sokolov 2002b), and laboratory experiments of 2D turbulence (Jullien et al. 1999). Although (12b) and (12c) are jus-

tified from dimensional arguments (Obukhov 1941a, b; Batchelor 1950), (12a) cannot be theoretically derived but rather is obtained by analogy with diffusion (Richardson 1926).

In the 2D turbulent enstrophy cascade, length scales smaller than the injection scale of the turbulence where $E(k) \sim k^{-3}$, the relative dispersion and diffusivity, scale as (Lin 1972)

$$[D^{(r)}(t)]^2 \sim \exp(t),$$
$$\kappa^{(r)} \sim [D^{(r)}]^2. \tag{13}$$

These scalings (13) have been recently observed in laboratory experiments of 2D turbulence (Jullien 2003). At long times, when particle separations are much larger than the largest eddies, the particles move independently and the relative dispersion asymptotes to absolute dispersion; that is,

$$\frac{1}{2}[D^{(r)}]^2 \rightarrow [D^{(a)}]^2, \tag{14}$$

and both scale as $\sim t^1$. For random spatially and temporally correlated velocity fields (i.e., at the smallest separations), it is straightforward to show that $[D^{(r)}]^2 \sim t^2$ and $\kappa^{(r)} \sim D^{(r)}$.

Unlike single-particle statistics, whose primary utility is quantifying eddy fluxes for the ensemble-averaged tracer evolution, two-particle statistics are primarily useful for determining the structure of the flow field (turbulent or not). However, similar to the ensemble-averaged patch, the spreading of the "typical" tracer patch [i.e., $P^{(r)}$] can be modeled by a diffusion-like equation with two-particle statistics quantifying the patch spreading (see Richardson 1926; Kraichnan 1966; Spydell et al. 2007).

The concept of 2D turbulence and the associated Lagrangian relative dispersion are based on a constant depth fluid. Depth variation will affect the vorticity dynamics central to 2D turbulence and lead to a non-isotropic, nonhomogeneous turbulence. Thus, the surf zone eddy field will not strictly follow canonical 2D turbulence. However, in general the surf zone bottom slope (here 0.025) is small, and these 2D turbulence concepts (both Eulerian and Lagrangian signatures) will be compared to the observed and modeled two-particle statistics.

5. Model–data comparison: Eulerian statistics

Prior to comparing observed and modeled Lagrangian statistics, an Eulerian wave and current comparison is
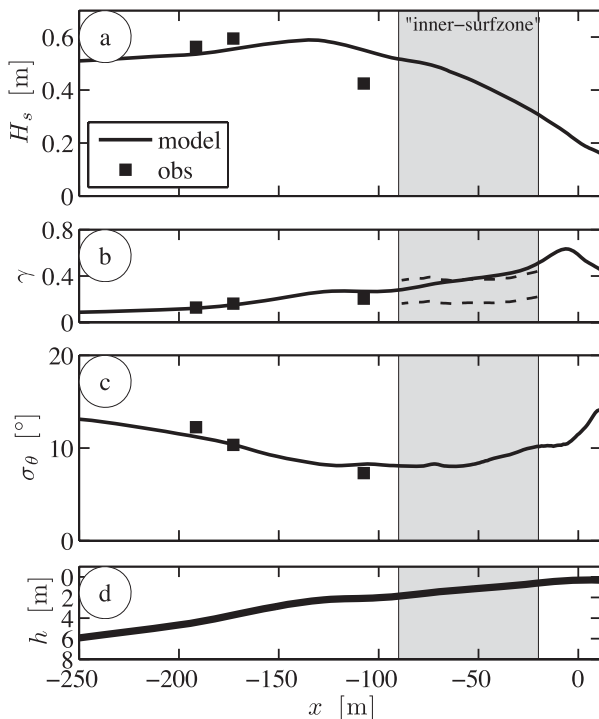
FIG. 3. The observed (squares) and modeled (lines) Eulerian wave statistics vs cross-shore coordinate x: (a) significant wave height H_s, (b) the significant wave height to total water depth d ratio $\gamma = H_s/d$, (c) directional wave spread σ_θ, and (d) the observed water depth h. The inner surf zone region ($-90 < x < -20$) is shaded. In (b) the total water depth d is mean depth h plus the mean setup $\bar{\eta}$. In addition, dashed lines in the inner surf zone indicate the previously observed (mean $\pm$ std dev) γ range (Raubenheimer et al. 1996).

performed. Wave statistics were observed at 3 ADV locations. The observed and modeled cross-shore variation of the significant wave height H_s compare well (Fig. 3a); however, the ADV locations are not ideal for a model test. Offshore $H_s = 0.5$ m and increases in shallower depths (Fig. 3d) because of shoaling until $x \approx -130$ m where H_s decreases. At the innermost ADV ($x = -107$ m), located in the outer surf zone, the model overpredicts H_s. There were no ADV observations in the inner surf zone ($-90 < x < -20$ m). Within the inner surf zone, modeled γ, the ratio of significant wave height to total water depth, gently increases (Fig. 3b) and is consistent with a γ parameterization (dashed curves in Fig. 3b), based on extensive field observations, which depend on local beach slope and kh (Raubenheimer et al. 1996). The waves are normally incident at all ADVs because the observed mean wave angle magnitude ($|\bar{\theta}| < 2°$) is within the ADV orientation error. The modeled waves are also normally incident with $|\bar{\theta}| < 1°$ at all cross-shore locations. The wave maker input was chosen so that the modeled and

observed σ_θ at the most offshore ADV were in approximate agreement. In the inner surf zone, modeled σ_θ increases (as observed in Herbers et al. 1999) and may result from surf zone eddies refracting waves, analogous to the increasing σ_θ due to shear-wave-induced wave refraction (Henderson et al. 2006). In addition to bulk (sea-swell integrated) moments (i.e., H_s), modeled and observed sea surface elevation spectra at the ADVs are in good agreement in the sea-swell band (not shown).

Observed and modeled drifter velocities are spatially binned and averaged to obtain Eulerian mean and fluctuating velocity statistics (Fig. 4). Modeled binned statistics are essentially alongshore uniform. The observed and modeled drifter-derived mean currents are weak (typically < 0.1 m s^{-1}; red arrows in Fig. 4). Within the inner surf zone at the $x = -60$ m bin, the alongshore-averaged mean alongshore current is 0.005 m s^{-1}, which is not significantly different from zero. Neither observed nor modeled mean cross-shore currents show any indication of long-lived rip currents. Similar to the model results of Johnson and Pattiaratchi (2006), short-lived ($\sim$100 s) episodic rip currents occurred in the model. The observed and modeled standard deviation ellipses are also consistent (green ellipses in Fig. 4). Seaward of the surf zone ($x < -150$ m), the cross-shore-directed shoaling surface gravity waves dominate the variance. Within the inner surf zone, low-frequency v fluctuations broaden the ellipses, although the modeled alongshore standard deviation is not as large as observed. The modeled maximum cross- and alongshore standard deviation velocities are 0.74 and 0.3 m s^{-1}, respectively, whereas the observed are 0.47 and 0.3 m s^{-1}, respectively.

The similarity between the observed and modeled bulk wave statistics up to the outer surf zone (Figs. 3a,c), the inner surf zone γ (Fig. 3b), and binned drifter velocities (Fig. 4) indicate that the Boussinesq model is reasonably representing surf zone processes. This is a prerequisite to a Lagrangian drifter dispersion model–data comparison. However, the Eulerian dataset is limited and more detailed Boussinesq model–data comparison with more extensive Eulerian field datasets will be performed.

6. Model–data comparison: Lagrangian statistics

a. Single particle (absolute) Lagrangian statistics

The modeled and observed drifter trajectories are used to calculate $P^{(r,a)}$, $[D^{(r,a)}]^2$, $\kappa^{(r,a)}$ as described in section 4 and compared with each other. The absolute displacement PDF $P^{(a)}(\mathbf{X}, a'_x, a'_y, t)$, with $\mathbf{X}$ being the inner surf zone bin ($-90 < x < -20$ m), was calculated
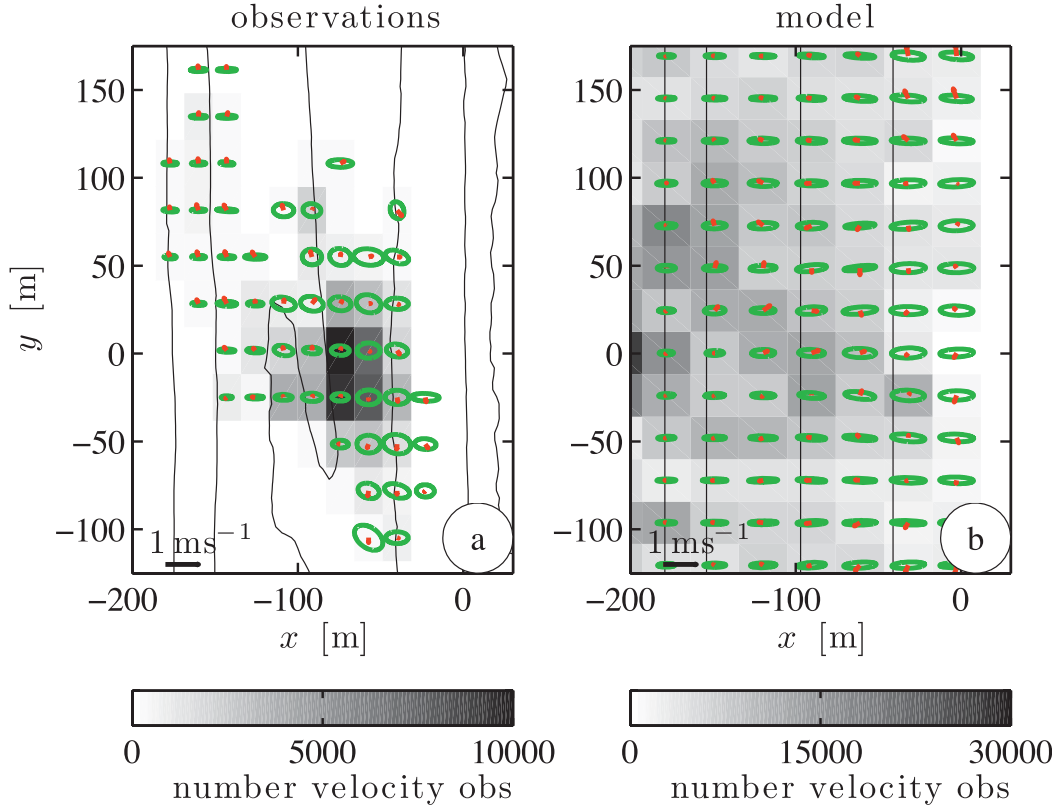
FIG. 4. Drifter derived mean (red arrows) and fluctuating (green std dev ellipses) currents as a function of x and y: (a) observations and (b) model, both superimposed on their respective bathymetries. The bins are 21 m $\times$ 25 m in x and y. The 1 m s^{-1} arrow is shown for reference. Only the 300-m alongshore span that overlaps the observed region is shown. The bin shading represents the total number (indicated by the color bars below) of (nonindependent) Lagrangian observations.

from both the observed and modeled displacements (Fig. 5). As discussed in Spydell et al. (2007), for $t \leq 16$ s, the observed $P^{(a)}$ is polarized in the cross-shore direction a'_x (first and second columns of Fig. 5) and alongshore a'_y polarized for $t \geq 64$ s (last column of Fig. 5). Thus, on average, a delta function tracer release initially spreads more quickly in the cross-shore direction, becomes roughly circular at $t \approx 16$ s, and subsequently elongates more rapidly in the alongshore. The observed and modeled $P^{(a)}$ are similar for all t (cf. the top and bottom panels of Fig. 5). At short times ($t = 1, 4$ s) the observed $P^{(a)}$ is broader in y and has more outliers in both x and y than modeled because of GPS position errors.

To further compare modeled and observed displacement PDFs, one-dimensional (1D) displacement PDFs are defined as

$$\bar{P}^{(a)}(a'_x) = \int_{-\infty}^{\infty} P^{(a)}(a'_x, a'_y) \, da'_y \qquad (15)$$

[and similarly for alongshore displacements, $\bar{P}^{(a)}(a'_y)$]. These 1D PDFs are then nondimensionalized by their

respective observed dispersion $D^{(a)}_{ij}$ so that PDF shapes at different times can be directly compared. Both observed and modeled nondimensional PDFs, for both along- and cross-shore displacements, approximately collapse to a Gaussian curve as expected for a 2D random flow field (Fig. 6). For the shortest time ($t = 1$ s), the modeled $\bar{P}^{(a)}(a'_x)$ is skewed toward $+a'_x$, because of steep waves (large $+u$ velocities) inducing large onshore $+a'_x$ displacements (Fig. 6a). GPS position error likely obscures this in the observations. For $t \geq 16$ s, both modeled and observed $\bar{P}^{(a)}(a'_x)$ have negatively skewed longer-than-Gaussian tails (i.e., at $> 2|a'_x|/D^{(a)}_{xx}$; Fig. 6a). This is because in the inner surf zone bin neither modeled nor observed drifters can have large $+a'_x$ displacements because drifters would end up beached, but large offshore $(-a'_x)$ displacements are possible. The nondimensional alongshore displacement PDFs $\bar{P}^{(a)}(a'_y)$ also deviate somewhat from Gaussian, with the modeled $\bar{P}^{(a)}(a'_y)$ having longer-than-Gaussian tails (Fig. 6b). The observed $\bar{P}^{(a)}(a'_y)$ is negatively skewed because of poor sampling, whereas the modeled
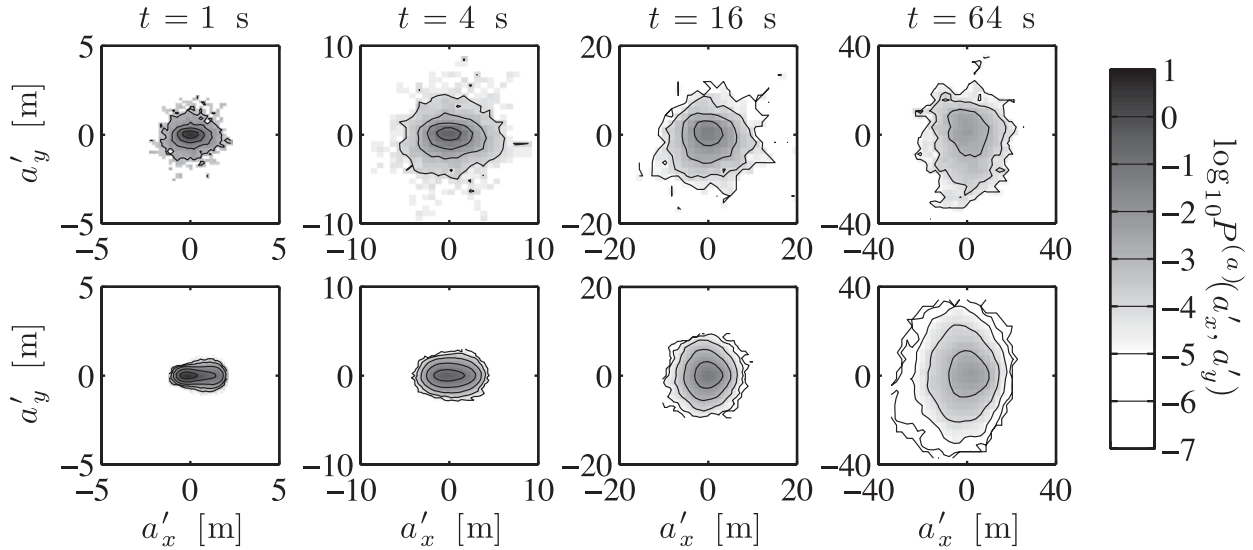
FIG. 5. The single particle displacement PDF $P^{(a)}(a'_x, a'_y, t)$ for the (top) observations and (bottom) model at four different times (from left to right, $t = 1$, 4, 16, and 64 s) in the inner surf zone bin. Note that the axis scale increases left to right.

$\bar{P}^{(a)}(a'_y)$ is symmetric for all t as expected for an along-shore uniform surf zone and normally incident waves.

Observed and modeled single-particle (absolute) cross- ($D^{(a)}_{xx}$) and alongshore ($D^{(a)}_{yy}$) dispersions are calculated for the inner surf zone bin as described in section 4. The observed and modeled $[D^{(a)}_{xx}]^2$ are similar (Fig. 7a). At $t < 5$ s, observed and modeled $[D^{(a)}_{xx}]^2$ have similar power laws (between 1 and 2). For $20 < t < 300$ s, the power law for the model becomes more ballistic (t^1 power law), whereas the one for the observations remains relatively unchanged from $t < 20$ s. Both observed and modeled $[D^{(a)}_{xx}]^2$ are Brownian (t^1 power law) for $t > 300$ s. The modeled and observed $[D^{(a)}_{xx}]^2$ have similar magnitudes for $t < 100$ s, and at later times ($200 < t < 1000$ s) the modeled is 1.5 to 3 times larger than observed—note that observed $[D^{(a)}_{xx}]^2$ is between 400 and 800 m² over this time. The observed and modeled $[D^{(a)}_{yy}]^2$ are also similar (Fig. 7b). Both modeled and observed $[D^{(a)}_{yy}]^2$ show ballistic ($20 < t < 300$ s) and Brownian regimes ($t > 600$ s). For $t < 200$ s the observed $[D^{(a)}_{yy}]^2$ is larger than the modeled, possibly due to GPS errors. Thereafter ($200 < t < 1000$ s), the modeled $[D^{(a)}_{yy}]^2$ is 1 to 2 times larger than the observed—observed $[D^{(a)}_{yy}]^2$ is between 1300 and 3000 m². The modeled and observed absolute diffusivities, $\kappa^{(a)}_{xx}$ and $\kappa^{(a)}_{xx}$ (7) for use in (10), are also similar (Fig. 8), particularly at shorter times ($t < 60$ s; Figs. 8a,b). At longer times, the modeled $\kappa^{(a)}_{xx}$ is larger than the observed and the modeled $\kappa^{(a)}_{yy}$ becomes approximately 2.5 times larger than the observed (Figs. 8c,d). Model diffusivity estimates seaward of the surf zone (see Spydell et al. 2007) are not discussed.

b. Two-particle (relative) Lagrangian statistics

One-dimensional separation PDFs $\bar{P}^{(r)}(r'_x)$ and $\bar{P}^{(r)}(r'_y)$ are defined similarly to the one-dimensional $\bar{P}^{(a)}$ (15). As previously found for the observations (Spydell et al. 2007), the modeled nondimensional separation PDFs $\bar{P}^{(r)}$ for small initial separations, $|\mathbf{R}_0| < 4$ m, follow Richardson scaling (12a) for all times (only $t < 256$ s is shown in Fig. 9, where there are a sufficient number of observations for quality comparison). However, the modeled separation PDFs become more Gaussian for larger $|\mathbf{R}_0|$ and longer times (not shown). As discussed in Spydell et al. (2007), the Richardson-scaled $\bar{P}^{(r)}$ (as opposed to the Gaussian) imply that drifter pairs do not move independently because of a self-similar interacting eddy field over a range of length scales. That the observed and modeled nondimensional $\bar{P}^{(r)}$ agree well for both cross- and alongshore separations (Figs. 9a and 9b, respectively) indicates that observed and modeled surf zone eddy field separating drifters are similar.

The observed and modeled cross- $[D^{(r)}_{xx}]^2$ and along-shore relative dispersions— $[D^{(r)}_{yy}]^2$, respectively—are calculated for the inner surf zone region from drifter separations as described in section 4b. Unlike the absolute dispersion, the modeled $[D^{(r)}_{xx}]^2$ is less than the observed for all times (Figs. 10a,b). The largest differences occur for small times and small $[D^{(r)}_{xx}]^2$ (< 10 m²), in part because of GPS position errors (± 1 m). The modeled $[D^{(r)}_{xx}]^2$ grows slowly on wave period time scales ($t < 20$ s), which is also seen, albeit less strongly, in the observations (Fig. 10a). For times $t > 300$ s, both observed and modeled $[D^{(r)}_{xx}]^2$ and $[D^{(r)}_{yy}]^2$ have greater
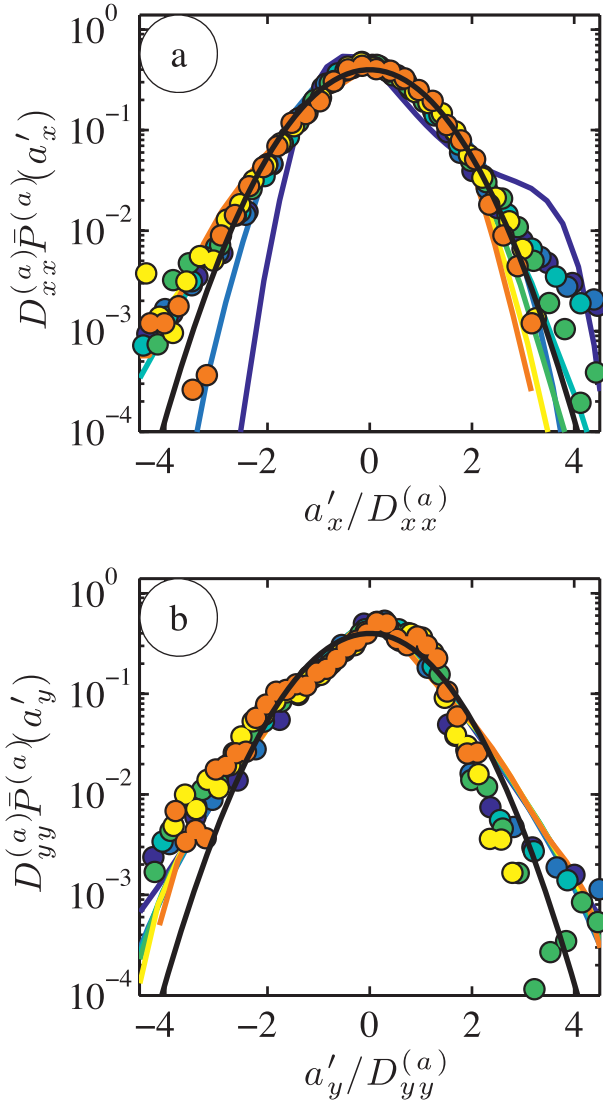
FIG. 6. Observed (dots) and modeled (curves) PDF $\bar{P}^{(a)}$ of absolute (a) x displacements a'_x and (b) y displacements a'_y at times $t = 1, 4, 16, 64, 128, 256$ s (colors from blue to orange). Both the PDFs and displacements are scaled by the std dev of the displacements at that time, $D_{xx}^{(a)}$ and $D_{yy}^{(a)}$, respectively. Only times out to $t = 256$ s are shown to minimize sampling error in the observed $\bar{P}^{(a)}$. The Gaussian (solid black lines) distribution is indicated.

FIG. 7. Observed (dashed) and modeled (solid) single particle dispersions (a) $[D_{xx}^{(a)}]^2$ and (b) $[D_{yy}^{(a)}]^2$ vs time t. Both t^1 and t^2 scalings are indicated as thin lines.

than t^2 power-law dependence, although this strong time dependence is not as clear in the observations. This indicates the presence of a 2D turbulent-like velocity field with a range of eddy sizes (Spydell et al. 2007). Diagnosing whether the modeled $[D_{xx}^{(r)}]^2$ and $[D_{yy}^{(r)}]^2$ follow inverse-energy ($\sim t^3$) or enstrophy ($\sim e^t$) cascade scalings is difficult from Figs. 10a,b.

Examination of the modeled relative diffusivity dependence on the relative dispersion shows that $\kappa_{xx}^{(r)} \sim [D_{xx}^{(r)}]^2$ for $10 < D_{xx}^{(r)} < 20$ m and $\kappa_{yy}^{(r)} \sim [D_{yy}^{(r)}]^2$ for
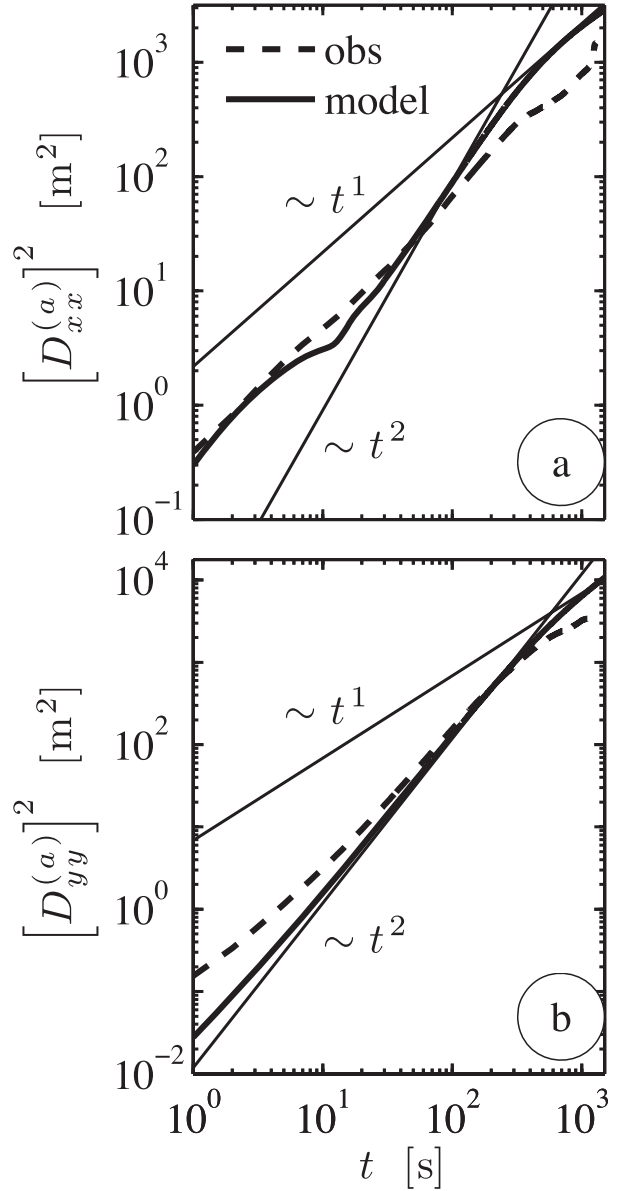
$5 < D_{yy}^{(r)} < 25$ m (gray thick lines in Figs. 10c,d), indicating enstrophy cascade scaling (13). At these length scales, $[D^{(r)}]^2$ should grow exponentially (gray thick lines in Figs. 10a,b). However, detecting this is difficult because it occurs for such a small range of length scales. For length scales smaller than the onset of enstrophy cascade scaling [$D^{(r)} \leq 5$ m], modeled and observed $\kappa_{yy}^{(r)} \sim [D_{yy}^{(r)}]^1$, as expected for purely random but correlated velocity fields. Both modeled $\kappa_{xx}^{(r)}$ and $\kappa_{yy}^{(r)}$ are weakly scale dependent at length scales between $25 < D^{(r)} < 40$ m but become at least $\kappa^{(r)} \sim [D^{(r)}]^1$ for length
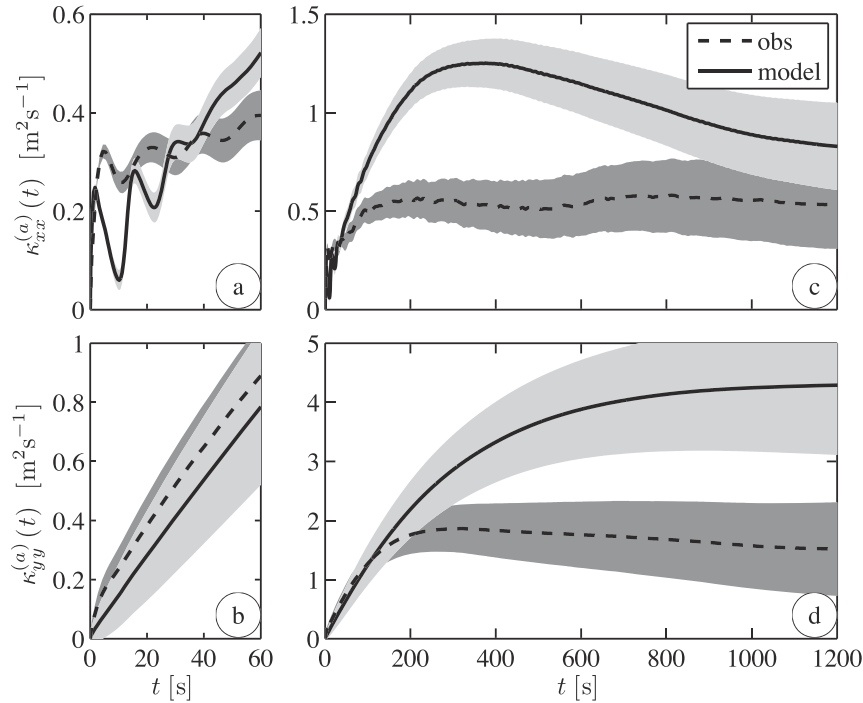
FIG. 8. Observed (dashed) and modeled (solid) single particle diffusivity (a),(c) $\kappa_{xx}^{(a)}$ and (b),(d) $\kappa_{yy}^{(a)}$ vs time t. The small time ($t < 60$ s) behavior is shown in (a) and (b). Shading indicates the error estimate (see Spydell et al. 2007).

scales larger than 40 m. At these larger length scales, the $[D^{(r)}]^2$ appears to scale $\sim t^3$ for $t > 1000$ in both x and y, an indicator of a 2D turbulent inverse-energy cascade.

Overall, modeled and observed two-particle statistics are comparable. In particular, the observed and modeled separation PDF shapes are very similar (Fig. 9). This, combined with the similar power-law scalings for the relative dispersion and the scale-dependent diffusivities (despite quantitative disagreement), indicates that in both the model and observations there is a turbulent eddy field with a range of length scales. The similarity between modeled and observed Lagrangian statistics justifies using the model to investigate the underlying processes driving surf zone Lagrangian dispersion.

7. Velocity-decomposed dispersion

Any two-dimensional velocity field can be written as the sum of an irrotational velocity due to velocity potential ϕ and the rotational velocity due to the curl of the streamfunction ψ; that is,

$$\mathbf{u} = \nabla\phi + \nabla \times \psi, \qquad (16)$$

where ∇ is the two-dimensional gradient operator. The irrotational velocity $\mathbf{u}_\phi = \nabla\phi$ is the divergent part of the flow and the rotational velocity $\mathbf{u}_\psi = \nabla \times \psi$ can have nonzero vorticity. For the $\sigma_\theta = 14°$ model run, the full model velocity field was output every $\Delta t = 0.5$ s for 5000 s after model spin-up. From this, ϕ and ψ are calculated at each time step by solving the elliptic equations

$$\nabla^2\phi = \nabla \cdot \mathbf{u}, \quad \text{and} \quad \nabla^2\psi = \zeta, \qquad (17)$$

where the vorticity $\zeta = \nabla \times \mathbf{u}$. The alongshore boundary conditions for both ϕ and ψ are periodic. At the onshore boundary, $\psi = 0$ and $\partial_x\phi = 0$. At the offshore boundary, $\psi = \int \langle v \rangle \, dx$ and $\phi = \int \langle u \rangle \, dx$, where $\langle \rangle$ represents an alongshore average. Both boundaries are within the sponge layer. From ϕ and ψ, $\mathbf{u}_\phi$ and $\mathbf{u}_\psi$ are estimated. The resulting root-mean-square (rms) errors (averaged in time, the alongshore, and over the region where drifters were released, $-240 < x < 0$ m) from the velocity decomposition are small: rms[$|\mathbf{u} - (\mathbf{u}_\phi + \mathbf{u}_\psi)|$] < 0.01 m s^{-1}.

At sea-swell frequencies ($0.05 < f < 0.3$ Hz), the velocities are largely irrotational. The $\mathbf{u}$ and $\mathbf{u}_\phi$ spectra are nearly identical for both cross- and alongshore (Fig. 11) components and are two or more orders of magnitude larger than the $\mathbf{u}_\psi$ spectra. The $\mathbf{u}_\phi$ velocities are dominated by variability at sea-swell frequencies. The modeled rotational motions are dominated by low frequencies and the $\mathbf{u}_\psi$ spectra are red. At low frequencies ($f < 0.005$ Hz), the full $\mathbf{u}$ and $\mathbf{u}_\psi$ spectra are similar
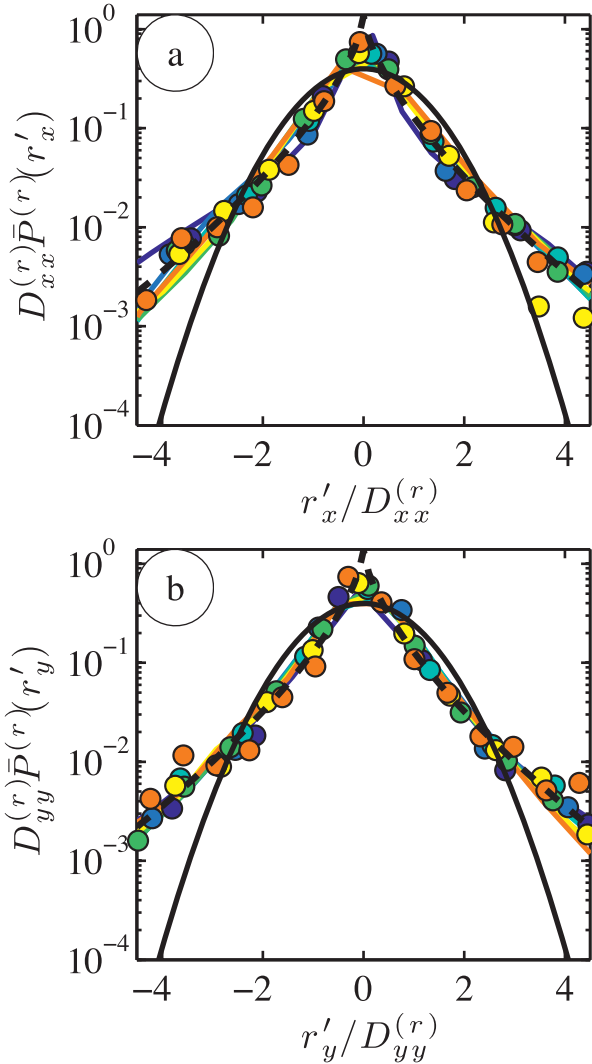
FIG. 9. Observed (dots) and modeled (curves) PDF $\bar{P}^{(r)}$ of relative (a) x separations r'_x, and (b) y separations r'_y at times $t = 1, 4, 16, 64, 128,$ and 256 s (colors from blue to orange). Both the PDFs and displacements are scaled by the std dev of separations at that time— $D^{(r)}_{xx}$ and $D^{(r)}_{yy}$, respectively. Only times out to 256 s are shown to minimize sampling error in the observed $\bar{P}^{(r)}$. Richardson [$\sim\exp(-|r'|^{2/3})$, dashed black lines] and Gaussian (solid black lines) distributions are indicated.

(gray and thick curves in Fig. 11) and are larger than the $\mathbf{u}_\phi$ spectra. A snapshot of the modeled vorticity is shown in Fig. 2b.

Drifters are seeded into and advected with the full $\mathbf{u}$, irrotational $\mathbf{u}_\phi$, and rotation $\mathbf{u}_\psi$ velocity fields. Examples of 1000-s-long drifter tracks from the three velocity fields are shown in Fig. 12. Overall, the $\mathbf{u}_\psi$-advected drifter tracks are smooth, have large (50–100 m) displacements (Fig. 12b), and visually appear as low-passed full $\mathbf{u}$ drifter tracks (Fig. 12a). The $\mathbf{u}_\phi$-advected drifter tracks have much smaller displacements and are

dominated by oscillations induced by high-frequency surface gravity waves (Fig. 12c). These oscillations are also observed in the full $\mathbf{u}$ drifter displacements (Fig. 12a). Note that the sum of the $\mathbf{u}_\phi$-advected and $\mathbf{u}_\psi$-advected drifter trajectories do not and should not equal the full model $\mathbf{u}$ trajectories.

Inner surf zone absolute $D^{(a)}$ and relative $D^{(r)}$ drifter dispersions are calculated for each of the three velocity fields (Fig. 13). Results for $[D^{(r)}]^2$ are shown for the $\mathbf{u}$, $\mathbf{u}_\phi$, and $\mathbf{u}_\psi$ velocity fields. The results are qualitatively similar for the decomposed absolute dispersion $[D^{(a)}]^2$. At short times ($t < 10$ s), the cross-shore $[D^{(r)}_{xx}]^2$ dispersion for the full $\mathbf{u}$ is nearly identical to the $\mathbf{u}_\phi$ dispersion (blue and red curves in Fig. 13a), resulting from random surface gravity waves. This is consistent with the $\mathbf{u}_\phi$ spectra dominant at $f > 0.05$ Hz. However, at longer time scales ($t > 100$ s), the $\mathbf{u}_\psi$-induced $[D^{(r)}_{xx}]^2$ asymptotes to the full $\mathbf{u}$ dispersion (blue and green curves in Fig. 13a), where the $\mathbf{u}_\phi$-induced $[D^{(r)}_{xx}]^2$ is two orders of magnitude smaller. The full $\mathbf{u}$ dispersion $[D^{(r)}_{yy}]^2$ follows the $\mathbf{u}_\psi$ dispersion for all times $t > 10$ s (Fig. 13b). These results demonstrate that surf zone dispersion is dominated by rotational motions and the $[D^{(r)}]^2$ power-law time dependence suggests 2D turbulent-like motions. Specifically, the relative dispersion for $t > 100$ s, when $\mathbf{u}_\psi$ dominates, includes both enstrophy cascade scaling—$[D^{(r)}]^2 \sim \exp(t)$; gray shaded region in Fig. 13—and inverse-energy cascade scaling—$[D^{(r)}]^2 \sim t^3$; dashed line in Fig. 13. At $t > 2000$ s, both the full $\mathbf{u}$ and $\mathbf{u}_\psi$-relative dispersions $[D^{(r)}]^2$ still have not fully asymptoted (14) to the $\mathbf{u}$ absolute dispersion $[D^{(a)}]^2$ (solid black curve in Fig. 13), indicating that the largest cross- $[D^{(r)}_{xx}]$ and alongshore $[D^{(r)}_{yy}]$ separations (33 and 100 m, respectively) are not large enough for the drifters to move independently.

The asymptotic ballistic (8) and Brownian (9) regimes for surf zone absolute dispersion $[D^{(a)}]^2$ are examined. The asymptotic diffusivity depends only on two quantities, the Lagrangian energy E_{ij} and time scale $T_{L,ij}$. Because the dispersion for $t > O(10)$ s is dominated by rotational velocities, the E_{ij} used is derived only from rotational velocities; that is,

$$E^{(\psi)}_{ij} = \frac{1}{2}\langle v'^{(\psi)}_i v'^{(\psi)}_j \rangle. \tag{18}$$

The irrotational surface gravity wave contribution to E_{ij} is not included because although its zero-lag Lagrangian velocity covariance (e.g., $E^{(\bar\phi)}_{ij}$) is substantial, irrotational motions do not contribute to the long-time dispersion. Thus, using the full E_{ij}, and known Lagrangian time scale results in asymptotic diffusivity predictions that are too large (because $\kappa^{(a)\infty}_{ij} = E_{ij}T_{L,ij}/2$). The
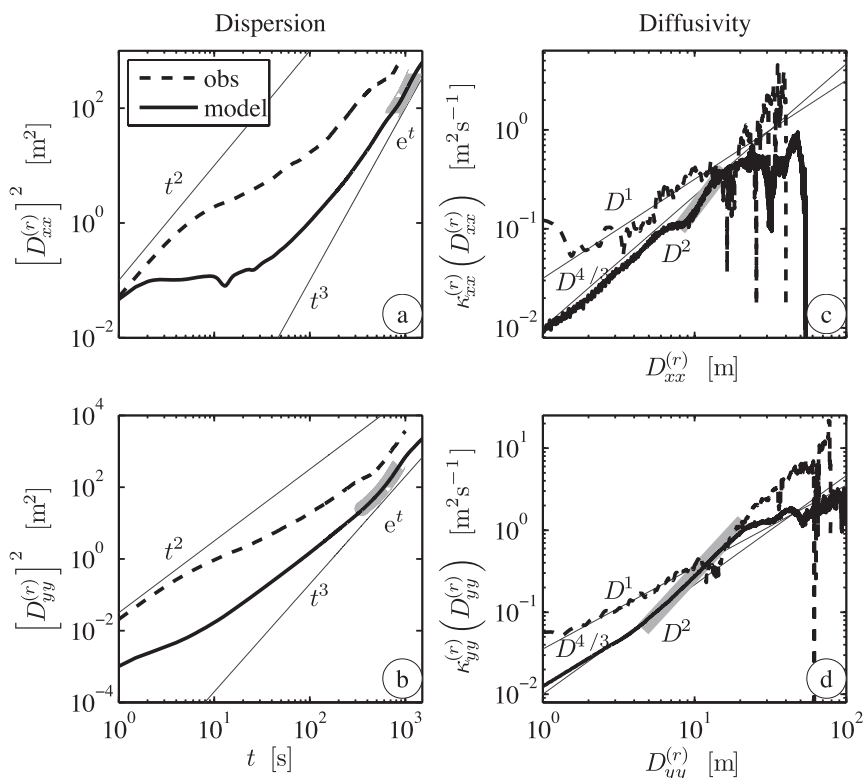
FIG. 10. (a),(b) The relative dispersion (a) $[D_{xx}^{(r)}]^2$ and (b) $[D_{yy}^{(r)}]^2$ vs time t and (c),(d) the relative diffusivity (c) $\kappa_{xx}^{(r)}$ and (d) $\kappa_{yy}^{(r)}$ vs separation $D^{(r)}$— $D_{xx}^{(r)}$ and $D_{yy}^{(r)}$, respectively—for initial separations $|R_0| < 4$ m. Observations are dashed lines and model results are solid lines. Power-law scalings are indicated as thin solid lines. The enstrophy cascade scalings (13) are indicated as thick gray lines.

Lagrangian time scale is then calculated from (9b) using the particle-derived $\kappa_{ij}^{(a)\infty}$ (see Fig. 8) and the $E_{ij}^{(\psi)}$; that is,

$$T_{L,ij} = \kappa_{ij}^{(a)\infty}/2E_{ij}^{(\psi)}.$$

Examining only the diagonal components, with $\kappa^{(a)\infty} =$ [0.75, 4.00] m^2 s^{-1} and $E_{ij}^{(\psi)} =$ [0.005, 0.006] m^2 s^{-2}, yields $T_L =$ [75, 333] s, considerably longer than $T_L =$ [7, 54] s for the day one observations (Spydell et al. 2007). This discrepancy results from the including irrotational velocities in E_{ij} used to calculate the observed T_L. With the $\mathbf{u}_\psi$-derived T_L and $E_{ij}^{(\psi)}$, both the ballistic and Brownian regimes for the modeled $[D^{(a)}]^2$ are well predicted (see dashed t and t^2 lines in Fig. 13), except for $[D_{xx}^{(a)}]^2$ for $t < 10$ s, which is surface gravity wave dominated. This further demonstrates the dominance of vorticity (rotational motions) in absolute as well as in relative dispersion.

8. Surf zone eddies, vorticity variability, and directional wave spread

As shown in section 7, dispersion is dominated by rotational (vorticity) motions (i.e., surf zone eddies)

rather than irrotational ones. The mechanism by which surf zone eddies are generated and how drifter dispersion is influenced is now addressed. In general, surf zone eddies have many possible generation mechanisms. Shear waves generate surf zone vorticity variability (Oltman-Shay et al. 1989), which in numerical models can spin up into eddies (e.g., Allen et al. 1996). However, shear waves require significant mean alongshore current shear (e.g., Bowen and Holman 1989), which was not present for the normally incident waves on this day of observations. Alongshore bathymetric variability may also play a role in generating surf zone eddies. Very low-frequency ($f < 0.004$ Hz) rotational motions were observed to be coupled to a rip channel morphology (MacMahan et al. 2004). However, spatially and temporally variable radiation stress forcing (i.e., wave groups, which is essentially the wave-averaged result of a random directionally spread wave field) were required to properly model the underlying very low-frequency variability (Reniers et al. 2007). Similar to the modeling results of Johnson and Pattiaratchi (2006), here a rich surf zone rotational velocity field (e.g., Fig. 2b) is generated on an alongshore uniform bathymetry. As discussed in Peregrine (1998),
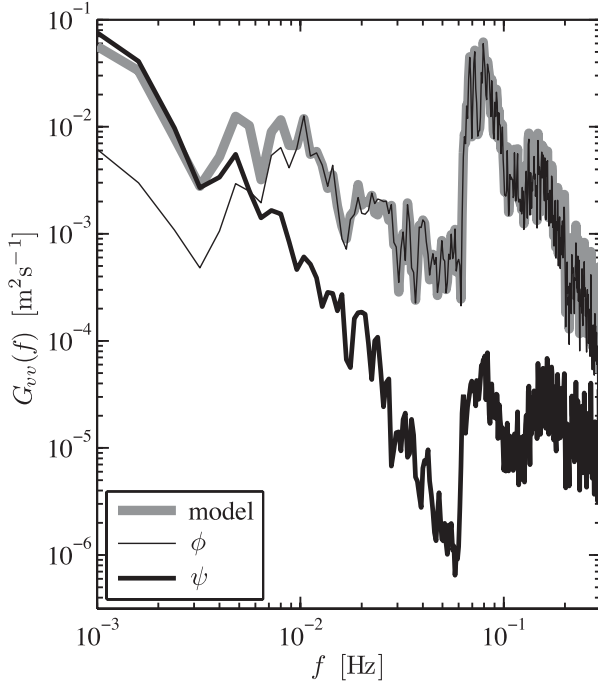
FIG. 11. Modeled alongshore velocity spectra $G_{vv}(f)$ vs frequency f for the full model $\mathbf{u}$, irrotational $\mathbf{u}_\phi$, and rotational $\mathbf{u}_\psi$ velocities (see legend) at $x = -60$ m. The features of the cross-shore velocity spectra are similar.

alongshore gradients in breaking wave heights act as a vorticity source in shallow water dynamics.

The effect of alongshore nonuniform wave breaking on vorticity is seen by taking the curl of (3) (neglecting higher-order terms), which results in

$$\frac{\partial \zeta}{\partial t} + \ldots = \mathbf{\nabla} \times \mathbf{F}_{br}, \qquad (19)$$

where the ellipsis $(\ldots)$ represents the standard vorticity advective and stretching terms. The curl of the dispersive $\{\mathbf{\nabla} \times \mathbf{F}_d = O[(kh)^2]\}$, bottom stress, and biharmonic friction terms in (3) are neglected. To see how this term acts as a vorticity source, consider normally incident waves with alongshore varying amplitude. As these waves enter the surf zone, depth-limited breaking only occurs where the waves are largest, thus resulting in finite crest-length broken waves and nonzero $\mathbf{F}_{br}$ (see schematic in Fig. 14). In this case, $\mathbf{F}_{br}$ is cross-shore (x) oriented and varies in the alongshore direction; thus, $\mathbf{\nabla} \times \mathbf{F}_{br}$ is nonzero, generating vorticity.

On alongshore uniform bathymetry, alongshore variable wave amplitude and thus finite breaking crest lengths are the result of directionally spread wave fields. The larger σ_θ is, the shorter the average breaking crest length. Surf zone vorticity, and hence Lagrangian dispersion, should then depend on the incident wave directional spread σ_{θ_0}. To test this idea, four additional model simulations with identical wave conditions except for the incident σ_{θ_0} were performed, resulting in five total runs to be analyzed with $\sigma_{\theta_0} = 0°, 4°, 7°, 14°, 20°$.

The $\sigma_{\theta_0} = 0°$ simulation is not realistic for a surf zone because there was zero alongshore velocity at all times due to the alongshore uniformity. No real beach has perfect alongshore uniform bathymetry and wave fields. However, the $\sigma_{\theta_0} = 0°$ run is interesting as an idealized example of the limit of infinite crest-length breaking

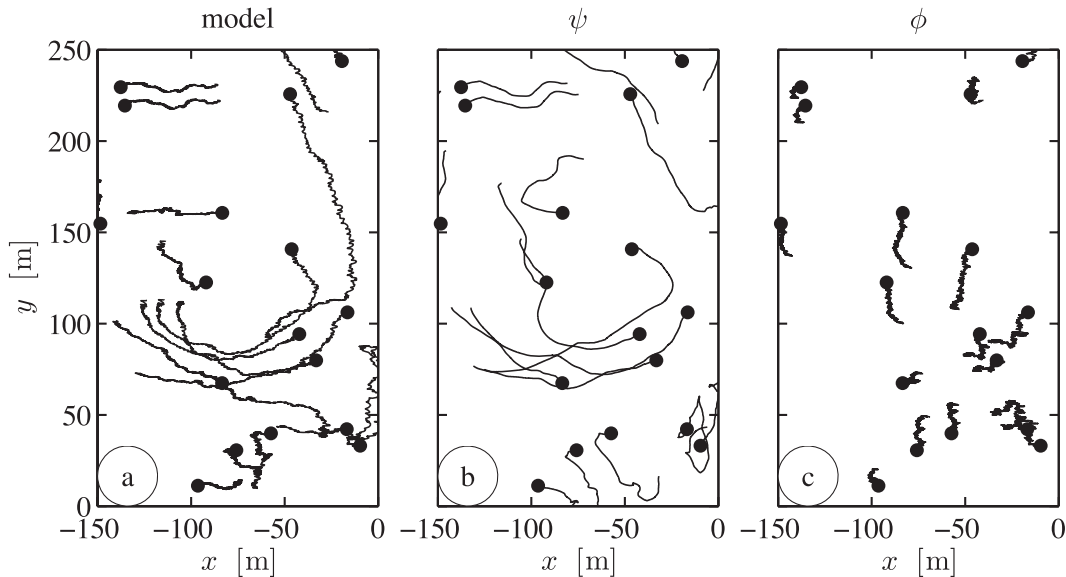FIG. 12. Modeled drifter tracks over 1000 s for (a) the modeled full velocity $\mathbf{u}$, (b) the rotational velocity $\mathbf{u}_\psi$, and (c) the irrotational velocity $\mathbf{u}_\phi$. The solid dot indicates the drifter initial position.
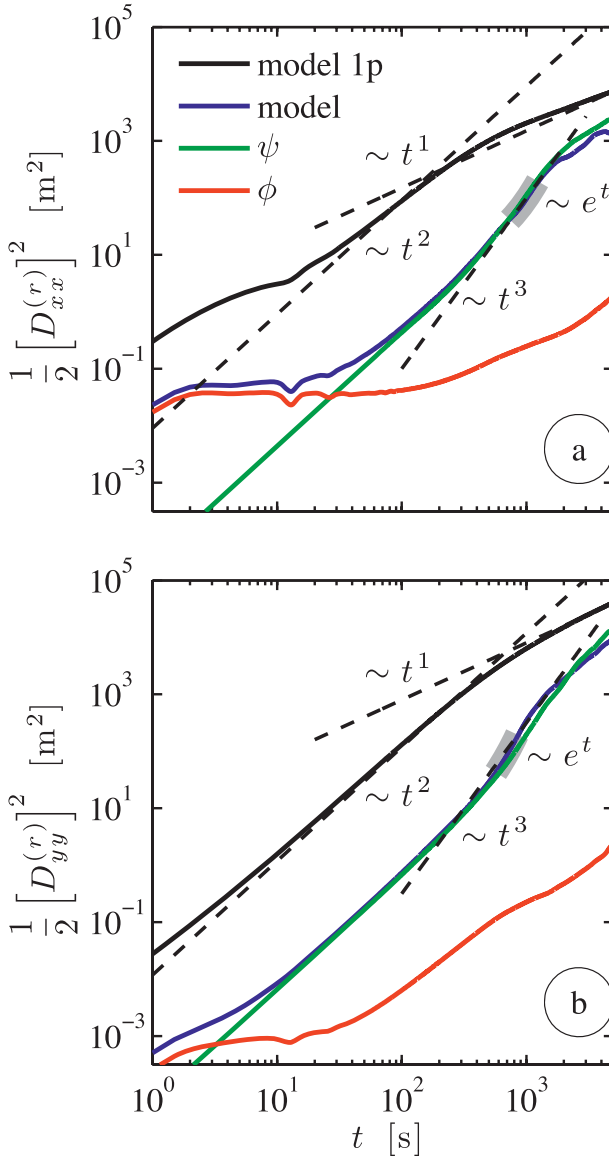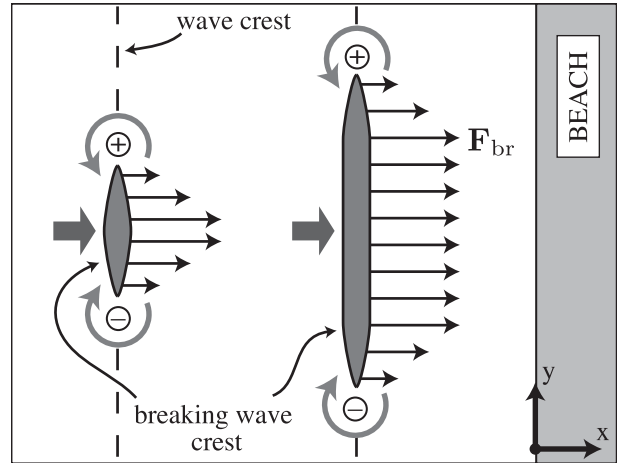
FIG. 14. Simplified schematic of finite breaking crest-length vorticity generations. Normally incident finite crest-length breaking waves approach the beach and the breaking crest length gets longer closer to the beach. The Boussinesq model breaking-wave force $\mathbf{F}_{br}$ is cross-shore oriented and is alongshore variable. This results in a nonzero $\nabla \times \mathbf{F}_{br}$ generating positive and negative vorticity at the crest ends (e.g., Peregrine 1998).

FIG. 13. Modeled relative dispersion (a) $(1/2) [D_{xx}^{(r)}]^2$ and (b) $(1/2) [D_{yy}^{(r)}]^2$ vs time t for the full model $\mathbf{u}$, $\mathbf{u}_\phi$, and $\mathbf{u}_\psi$-advected drifters as indicated in the legend. The $[D^{(a)}]^2$ derived from the full model $\mathbf{u}$ also is shown in black. The asymptotic ballistic and Brownian scalings are shown as the t^1 and t^2 dashed lines, as is the Richardson scaling $D^{(r)} \sim t^3$. The enstrophy cascade scaling $[D^{(r)}]^2 \sim e^t$ is indicated as the gray region over the same range as in Fig. 10.

waves. This simulation clearly resulted in no vorticity generation and negligible (single- and two-particle) drifter dispersion. Results from this simulation are thus not shown.

The cross-shore dependence of the wave spread σ_θ is similar for each of the different $\sigma_{\theta_0} = 4°, 7°, 14°,$ and $20°$ simulations (Fig. 15a). For each σ_{θ_0}, the wave spread

decreases as the surf zone is approached and then, for all but the $\sigma_{\theta_0} = 20°$ simulation, increases through the inner surf zone until the shore is reached. Recall that for the $\sigma_{\theta_0} = 14°$ run, the modeled $\sigma_\theta(x)$ matched the observations (see also Fig. 3c). The mean vorticity for all σ_{θ_0} is zero at all x because bores can only generate (potential) vorticity anomalies (Bühler 2000). However, the model vorticity standard deviation std(ζ) (based on a time- and alongshore average) increases with larger incident σ_{θ_0} (Fig. 15b) and also increases within the inner surf zone where the majority of wave dissipation occurs. Similarly, Kennedy (2005) showed that increasing σ_θ increases the magnitude of the fluctuating rotational velocities. Well offshore of the surf zone ($x < -200$ m) the vorticity variability is small because few eddies generated in the surf zone were able to propagate that far offshore.

Inner surf zone vorticity wavenumber spectra $G_{\zeta\zeta}(k_y)$ are constructed for all σ_{θ_0} by averaging the instantaneous vorticity alongshore wavenumber periodogram over the inner surf zone ($-90 < x < -20$ m) and over t. For all σ_{θ_0}, $G_{\zeta\zeta}$ is red and spread over a large range of alongshore wavenumbers k_y (Fig. 16). For $k_y > 5 \times 10^{-3}$ cpm (cycles per meter), $G_{\zeta\zeta}$ is larger for increasing σ_{θ_0}. Thus, the increased vorticity variability with larger σ_{θ_0} (Fig. 15) is spread over 10–200-m length scales. For all σ_{θ_0}, $G_{\zeta\zeta}$ appears to have two differing wavenumber dependencies. Specifically, for the $\sigma_{\theta_0} = 14°$ and $20°$ runs, $G_{\zeta\zeta}$ falls off very rapidly for $k_y > 0.05$ cpm and more gently for $0.01 < k_y < 0.05$ cpm; that is, at the

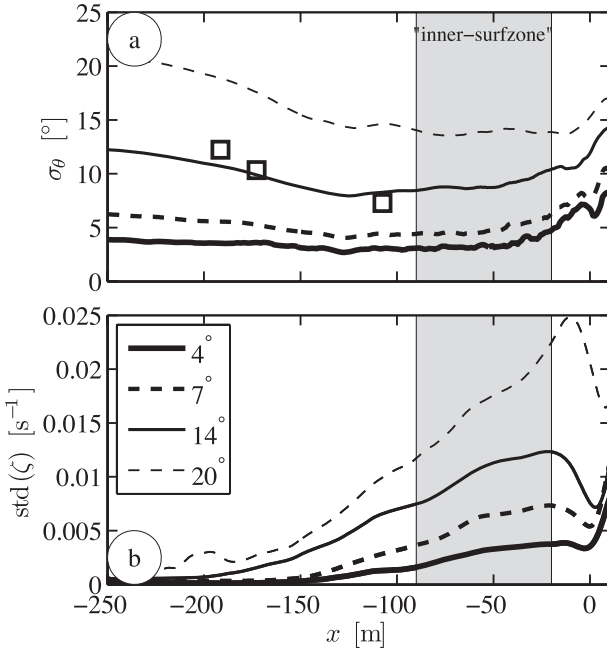FIG. 15. Modeled (a) wave directional spread σ_θ and (b) vorticity std dev (ζ) vs x for different incident directional spreads σ_{θ_0}. The open squares in (a) are the ADV observations.
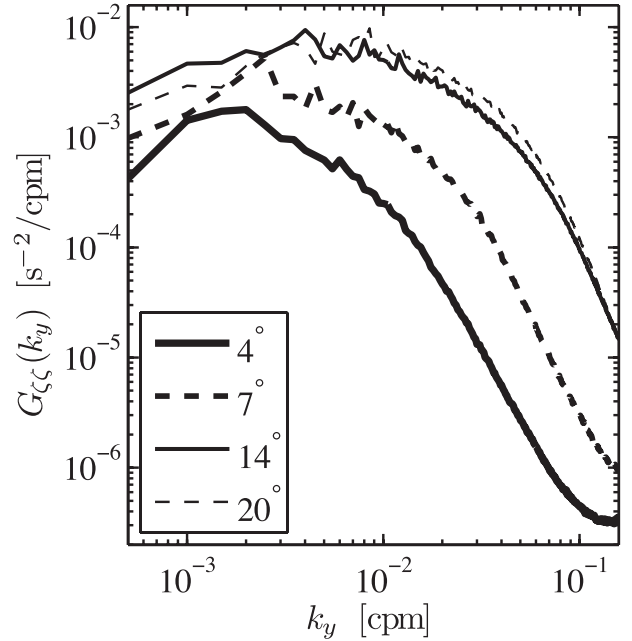

FIG. 16. Surf zone vorticity alongshore wavenumber spectrum $G_{\zeta\zeta}$ vs alongshore cyclic wavenumber k_y for various incident σ_{θ_0} (see legend). The spectra $G_{\zeta\zeta}$ are averaged in x across the inner surf zone region.

transitional wavenumber $k_y \approx 0.05$ cpm, the $G_{\zeta\zeta}$ power-law dependence changes. The two other σ_{θ_0} runs also show two $G_{\zeta\zeta}(k_y)$ regimes, but with a smaller transitional wavenumber for decreasing σ_{θ_0}, consistent with longer breaking crest lengths injecting energy at longer length scales.

The increased vorticity variability induced by increasing σ_{θ_0} also results in larger inner surf zone–relative dispersion (Fig. 17). For $t < 10$ s, the cross-shore dispersion $[D_{xx}^{(r)}]^2$ is similar for all σ_{θ_0} (Fig. 17a) because these time scales are too short for vorticity motions to separate drifters. At longer times $t > 10$ s, $[D_{xx}^{(r)}]^2$ is larger with increasing σ_{θ_0} as surf zone eddies separate the drifters. In addition, for larger σ_{θ_0}, significant cross-shore drifter separation $[D_{xx}^{(r)}]^2$ begins at earlier times as the increased vorticity variance (Fig. 15b) at smaller length scales increases (Fig. 16). At $t = 2000$ s, order of magnitude differences in $[D_{xx}^{(r)}]^2$ exist for the various σ_{θ_0}. For example, with $\sigma_{\theta_0} = 20°$ and 4°, drifters have cross-shore separated an average of $D_{xx}^{(r)} = 45$ m and $D_{xx}^{(r)} = 3.3$ m, respectively (Fig. 17a). In general, $[D_{yy}^{(r)}]^2$ is larger for increased σ_{θ_0} (Fig. 17b). The $[D_{yy}^{(r)}]^2$ power-law scaling is similar for all σ_{θ_0}, and only the magnitude varies. At times $10 < t < 1000$ s, the $\sigma_{\theta_0} = 20°$ $[D_{yy}^{(r)}]^2$ is slightly larger than for $\sigma_{\theta_0} = 14°$, whereas for $t > 1000$ s they are the same. Furthermore, the $\sigma_{\theta_0} = 14°$ and 20° runs have largely similar $G_{\zeta\zeta}(k_y)$ (Fig. 16), possibly indicating a vorticity saturation. The σ_{θ_0} dependence of

absolute dispersion is qualitatively similar to that of relative dispersion (not shown).

The modeled relative dispersion indicates the presence of a 2D turbulent enstrophy and inverse-energy cascade with an injection length scale of approximately 20 m for $\sigma_{\theta_0} = 14°$. Although the dispersive velocities are rotational and the vorticity is spread over wavenumber space, the 2D turbulent character of the modeled surf zone remains to be quantified from the Eulerian model data. An Eulerian statistic useful for classifying enstrophy and inverse-energy cascade regions is the velocity structure function $S_v(\Delta y)$, defined as

$$S_v(\Delta y) = \langle [v(y + \Delta y) - v(y)]^2 \rangle, \qquad (20)$$

where v is the instantaneous alongshore velocity and the average $\langle \cdot \rangle$ is over time and the alongshore direction y. In 2D turbulence, dimensional arguments (e.g., Kellay and Goldburg 2002), lead to

$$S_v(\Delta y) \sim (\Delta y)^{2/3}, \qquad L_0 > \Delta y > y_{in}$$
$$S_v(\Delta y) \sim \beta^{2/3}(\Delta y)^2, \qquad \Delta y < y_{in} \qquad (21)$$

for an inverse-energy and enstrophy cascade, respectively. In (21), L_0 is the largest length scale at which velocities are correlated, y_{in} is the injection length scale at which the 2D turbulence field is forced, β is the enstrophy injection rate, and ϵ is the energy injection
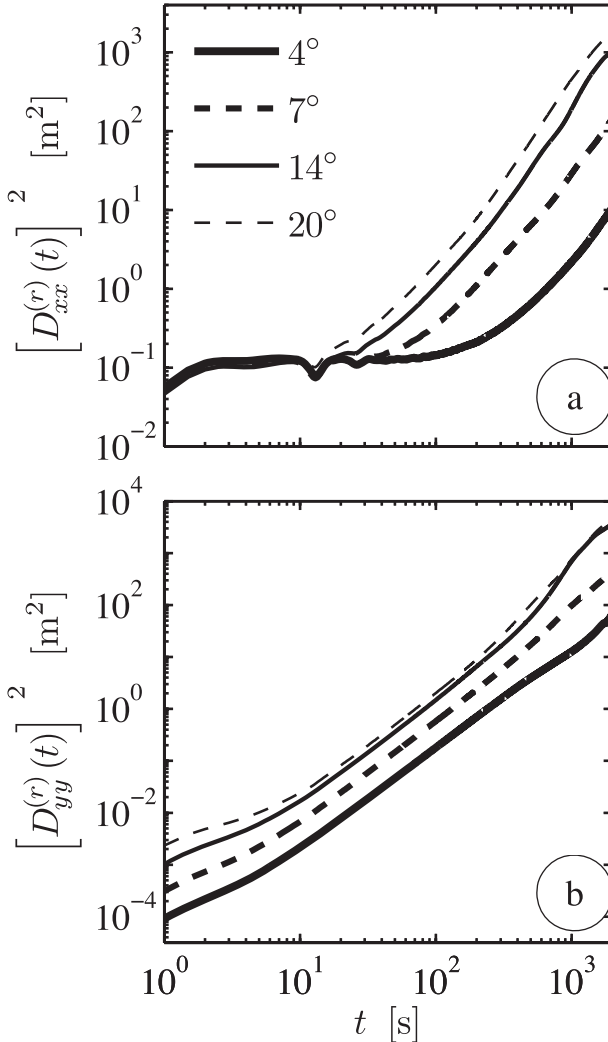
FIG. 17. Modeled two-particle relative dispersion (a) $[D_{xx}^{(r)}]^2$ and (b) $[D_{yy}^{(r)}]^2$ vs time t for the various incident σ_{θ_0} (see legend).

indicating the presence of an inverse-energy cascade region (gently sloping dashed line in Fig. 18c). The transition length scale y_{in} from enstrophy to inverse-energy cascades is 10–20 m, consistent with the transition scale inferred from the relative dispersion statistics (section 6b). At $\Delta y > L_0 = 200$ m, $S_v(\Delta y)$ approaches a constant because alongshore velocities at these separations are uncorrelated. Seaward of the surf zone (e.g., $x = -189$ m; thin lines in Fig. 18c), no inverse-energy cascade $[S_v \sim (\Delta y)^{2/3}]$ region is observed because there is no breaking wave vorticity injection. The other σ_{θ_0} runs exhibit similar behavior, but with weaker overall S_v and with y_{in} and L_0 increasing for decreasing σ_{θ_0}. This is consistent with the larger breaking crest-lengths injecting vorticity at larger length scales. The $\sigma_{\theta_0} = 4°$ run is unique in that there is no inverse-energy cascade region at any cross-shore locations.

From both Eulerian (structure function) and Lagrangian (relative dispersion) analysis, the modeled surf zone appears 2D turbulent-like. The turbulence magnitude (rms vorticity or relative dispersion) and the length scales L_0 and y_{in} depend on σ_{θ_0} ($y_{in} \approx 10$–20 m for the $\sigma_{\theta_0} = 14°$ simulation). For larger σ_{θ_0}, the modeled inner surf zone structure function follows inverse-energy cascade scaling [i.e., $S_v \sim (\Delta y)^{2/3}$] for $\Delta y > 20$ m (Fig. 18). This is consistent with the modeled relative dispersion because the nondimensionalized separation PDFs follow the Richardson scaling and $[D^{(r)}]^2 \sim t^3$ for $D^{(r)} > 20$ m (Fig. 17). Furthermore, the length scales for the enstrophy cascade are similar for the Eulerian ($\Delta y < 10$ m) and Lagrangian [$5 < D^{(r)} < 20$ m] analyses.

9. Summary

Surf zone drifter dispersion was observed on a beach with small normally incident directionally spread waves (Spydell et al. 2007). For these conditions, surf zone Lagrangian drifter dispersion was simulated with a time-dependent wave-resolving Boussinesq model. The limited observed Eulerian (wave properties, mean currents) statistics are well reproduced by the model. The model reproduces the observed absolute dispersion statistics with approximately Gaussian displacement PDFs and comparable along- and cross-shore dispersions (and diffusivities). The long-time model alongshore absolute diffusivities are 2.5 times larger than observed. The observed relative dispersion is reasonably well reproduced by the model. Both observed and modeled nondimensionalized separation PDFs are Richardson-like. The modeled $[D_{xx}^{(r)}]^2$ and $[D_{yy}^{(r)}]^2$ are smaller than observed. For short times, this is likely partially results from GPS error in the observations. The modeled and observed relative dispersions have approximately the same
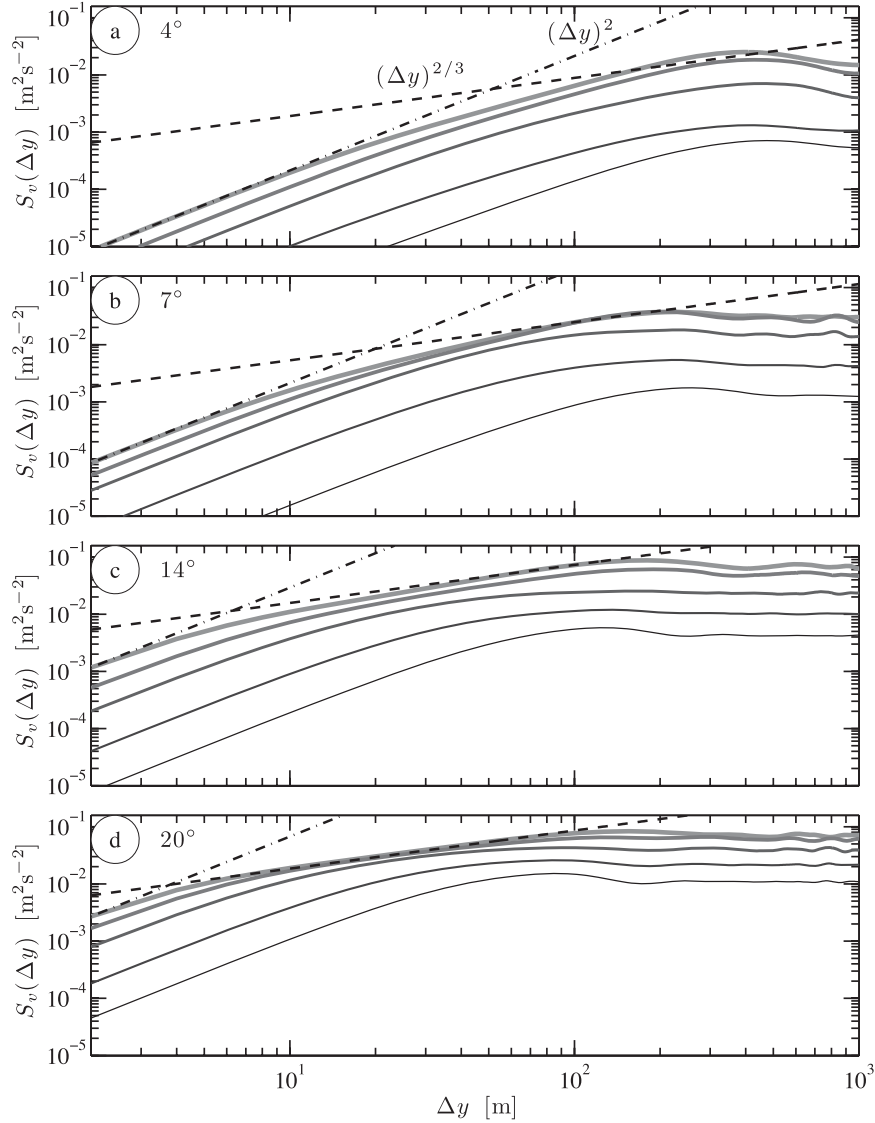
rate. The structure function scalings (21) are analogous to the $E \sim k_y^{-3}$ and $E \sim k_y^{-5/3}$ wavenumber spectra scalings for enstrophy and inverse-energy cascade regions, respectively. Note, however, that an $S_v \sim (\Delta y)^2$ scaling is also possible at small Δy for purely random but spatially correlated velocities. The structure function S_v (Δy) (20) is readily calculated for the different σ_{θ_0} at various x locations from the Boussinesq model Eulerian data (Fig. 18).

For the $\sigma_{\theta_0} = 14°$ run, $S_v(\Delta y)$ suggests an enstrophy and inverse-energy cascade (Fig. 18c). Specifically, for inner surf zone locations (e.g., $x = -34$ m), the structure function follows $S_v \sim (\Delta y)^2$ for approximately $\Delta y < 10$ m (steepest dashed line in Fig. 18c), suggesting the presence of an enstrophy cascade region. At larger scales, approximately $20 < \Delta y < 150$ m, $S_v \sim (\Delta y)^{2/3}$,

FIG. 18. The alongshore velocity structure function $S_v(\Delta y)$ vs Δy for the four different incoming wave spreads: σ_{θ_0} = (a) 4°, (b) 7°, (c) 14°, and (d) 20°. Shade (black to gray) and thickness (thin to thick) correspond to cross-shore locations $x = -189, -109, -59, -34, -9$ m.

power-law time dependence—stronger than $[D^{(r)}]^2 \sim t^1$—and the relative diffusivity has the same power law scale dependence: $k^{(r)} \sim [D^{(r)}]^n$ with $1 \leq n \leq 2$. Both enstrophy and inverse-energy cascade regions are identified in the modeled relative dispersion.

The model velocity field was decomposed into irrotational (surface gravity waves) and rotational (vorticity) motions. Higher-frequency ($f > 0.01$ Hz) motions are dominated by irrotational velocities, surface gravity waves, and lower-frequency ones ($f < 0.005$ Hz) by rotational velocities. Drifters are advected within the irrotational and rotational velocity fields. At times longer than $t \approx 30$ s, absolute and relative drifter dis-

persion are dominated by the rotational velocity field, indicating the importance of surf zone eddies (vorticity) in drifter dispersion. Alongshore gradients in breaking wave dissipation generate vorticity (e.g., Peregrine 1998) over a range of scales. On an alongshore uniform beach, a directionally spread wave field is required for finite breaking crest-lengths. Simulations with increased incident σ_{θ_0} result in increased rms vorticity over a broader range of length scales, giving rise to increased drifter dispersion. The velocity structure function $S_v(\Delta y)$ generally shows regions with both enstrophy and inverse-energy cascade scalings. For larger σ_{θ_0}, $S_v(\Delta y)$ magnitude increases and both the upper (L_0) and lower

(y_{in}, the injection scale of the turbulence) length scale limits of the inverse-energy cascade decreases. Both Eulerian [$S_v(\Delta y)$] and Lagrangian (two-particle) statistics reveal that the modeled surf zone is a quasi 2D-turbulent fluid. For the case where $\sigma_{\theta_0} = 14°$, these Eulerian and Lagrangian statistics generally indicate an enstrophy cascade (approximately 5–10-m length scales) and inverse-energy cascade (approximately 20–100-m length scales).

APPENDIX

Definition of Wave Statistics

The frequency directional sea surface elevation spectrum is given by $E_{\eta\eta}(f,\theta)$, where f is the frequency and θ the wave direction. The frequency spectrum $G_{\eta\eta}(f)$ is the integral over all directions,

$$G_{\eta\eta}(f) = \int_{-\pi}^{\pi} E_{\eta\eta}(f,\theta)\mathrm{d}\theta,$$

so that

$$\mathrm{Var}(\eta) = \int_0^{\infty} G_{\eta\eta}(f)\mathrm{d}f$$

and the significant wave height H_s is defined as

$$H_s = 4\left[\int_{SS} G_{\eta\eta}(f)\mathrm{d}f\right]^{1/2},$$

where the integral is over the sea-swell band (SS) of 0.05–0.3 Hz. The bulk (sea-swell band frequency-integrated) wave angle $\bar{\theta}$ and directional spread σ_θ are defined as (Kuik et al. 1988)

$$\bar{\theta} = \arctan\left[\frac{\int_{SS}\int_{-\pi}^{\pi}\sin(\theta)E_{\eta\eta}(f,\theta)\,\mathrm{d}\theta\,\mathrm{d}f}{\int_{SS}\int_{-\pi}^{\pi}\cos(\theta)E_{\eta\eta}(f,\theta)\,\mathrm{d}\theta\,\mathrm{d}f}\right] \quad \text{and}$$

$$\sigma_\theta^2 = \frac{\int_{SS}\int_{-\pi}^{\pi}\sin^2(\theta-\bar{\theta})E_{\eta\eta}(f,\theta)\mathrm{d}f\,\mathrm{d}\theta}{\int_{SS}\int_{-\pi}^{\pi}E_{\eta\eta}(f,\theta)\,\mathrm{d}f\,\mathrm{d}\theta}.$$

Direct estimates of the directional spectrum are not required to calculate $\bar{\theta}$ and σ_θ. Instead, both are functions of the lowest bulk Fourier directional moments a_2 and b_2 (Kuik et al. 1988), as described in Herbers et al. (1999), which depend on the u and v cross-spectra. For the field data these wave statistics are estimated from the u and v spectra converted with linear theory to sea surface elevation spectra, and for the model output, the η, u, and v spectra are similarly used.

REFERENCES

Allen, J., P. A. Newberger, and R. A. Holman, 1996: Nonlinear shear instabilities of alongshore currents on plane beaches. *J. Fluid Mech.,* **310,** 181–213.

Batchelor, G. K., 1950: The application of the similarity theory of turbulence to atmospheric diffusion. *Quart. J. Roy. Meteor. Soc.,* **76,** 133–146.

Boehm, A. B., S. B. Grant, J. H. Kim, C. D. McGee, S. Mowbray, C. Clark, D. Foley, and D. Wellmann, 2002: Decadal and shorter period variability of surf zone water quality at Huntington Beach, California. *Environ. Sci. Technol.,* **36,** 3885–3892.

Boffetta, G., and I. M. Sokolov, 2002a: Relative dispersion in fully developed turbulence: The Richarson's law and intermittency corrections. *Phys. Rev. Lett.,* **88,** 094501, doi:10.1103/PhysRevLett.88.094501.

——, and ——, 2002b: Statistics of two-particle dispersion in two-dimensional turbulence. *Phys. Fluids,* **14,** 3224–3282.

Bowen, A. J., and R. A. Holman, 1989: Shear instabilities of the mean longshore current. 1. Theory. *J. Geophys. Res.,* **94,** 18 023–18 030.

Bühler, O., 2000: On the vorticity transport due to dissipating or breaking waves in shallow-water flow. *J. Fluid Mech.,* **407,** 235–263.

Chen, Q., R. A. Dalrymple, J. T. Kirby, A. B. Kennedy, and M. C. Haller, 1999: Boussinesq modeling of a rip current system. *J. Geophys. Res.,* **104,** 20 617–20 637.

——, J. T. Kirby, R. A. Dalrymple, A. B. Kennedy, and A. Chawla, 2000: Boussinesq modeling of wave transformation, breaking, and runup. II: 2D. *J. Waterway Port Coastal Ocean Eng.,* **126,** 48–56.

——, ——, ——, F. Shi, and E. B. Thornton, 2003: Boussinesq modeling of longshore currents. *J. Geophys. Res.,* **108,** 3362, doi:10.1029/2002JC001308.

Clarke, L., D. Ackerman, and J. Largier, 2007: Dye dispersion in the surf zone: Measurements and simple models. *Cont. Shelf Res.,* **27,** 650–669.

Davis, R. E., 1987: Modeling eddy transport of passive tracers. *J. Mar. Res.,* **45,** 635–665.

——, 1991: Observing the general circulation with floats. *Deep-Sea Res.,* **38,** S531–S571.

Denny, M. W., and M. F. Shibata, 1989: Consequences of surf-zone turbulence for settlement and external fertilization. *Amer. Naturalist,* **134,** 859–889.

Doutt, J. D., G. V. Frisk, and H. Martell, 1998: Using GPS at sea to determine the range between a moving ship and a drifting buoy to centimeter-level accuracy. *Proc. OCEANS '98,* Nice, France, IEEE, 1344–1347.

Durran, D. R., 1991: The third-order Adams–Bashforth method—An attractive alternative to leapfrog time differencing. *Mon. Wea. Rev.,* **119,** 702–720.

Feddersen, F., 2007: Breaking wave induced cross-shore tracer dispersion in the surf zone: Model results and scalings. *J. Geophys. Res.,* **112,** C09012, doi:10.1029/2006JC004006.

——, and R. T. Guza, 2003: Observations of nearshore circulation: Alongshore uniformity. *J. Geophys. Res.,* **108,** 3006, doi:10.1029/2001JC001293.

——, ——, S. Elgar, and T. H. C. Herbers, 1998: Alongshore momentum balances in the nearshore. *J. Geophys. Res.,* **103,** 15 667–15 676.

George, R., and J. L. Largier, 1996: Description and performance of finescale drifters for coastal and estuarine studies. *J. Atmos. Oceanic Technol.,* **13,** 1322–1326.

Gobbi, M. F., J. T. Kirby, and G. Wei, 2000: A fully nonlinear Boussinesq model for surface waves. Part 2. Extension to $O(kh)^4$. *J. Fluid Mech.,* **405,** 181–210.

Grant, S., J. Kim, B. Jones, S. Jenkins, and J. Wasyl, 2005: Surf zone entrainment, along-shore transport, and human health implications of pollution from tidal outlets. *J. Geophys. Res.,* **110,** C10025, doi:10.1029/2004JC002401.

Haile, R. W., and Coauthors, 1999: The health effects of swimming in ocean water contaminated by storm drain runoff. *Epidemiology,* **10,** 355–363.

Harlow, F., and J. Welch, 1965: Numerical calculation of time-dependent viscous incompressible flow of fluid with free surfaces. *Phys. Fluids,* **8,** 2181–2189.

Harris, T., J. Jordaan, W. McMurray, C. Verwey, and F. Anderson, 1963: Mixing in the surf zone. *Int. J. Air Water Pollut.,* **7,** 649–667.

Henderson, S. M., R. T. Guza, S. Elgar, and T. H. C. Herbers, 2006: Refraction of surface gravity by shear waves. *J. Phys. Oceanogr.,* **36,** 629–635.

Herbers, T. H. C., S. Elgar, and R. T. Guza, 1999: Directional spreading of waves in the nearshore. *J. Geophys. Res.,* **104,** 7683–7693.

Inman, D., R. Tait, and C. Nordstrom, 1971: Mixing in the surf zone. *J. Geophys. Res.,* **26,** 3493–3514.

Jiang, S. C., and W. Chu, 2004: PCR detection of pathogenic viruses in Southern California urban rivers. *J. Appl. Microbiol.,* **97,** 17–28.

Johnson, D., and C. Pattiaratchi, 2004: Transient rip currents and nearshore circulation on a swell-dominated beach. *J. Geophys. Res.,* **109,** C02026, doi:10.1029/2003JC001798.

——, and ——, 2006: Boussinesq modelling of transient rip currents. *Coast. Eng.,* **53,** 419–439.

Jullien, M.-C., 2003: Dispersion of passive tracers in the direct enstrophy cascade: Experimental results. *Phys. Fluids,* **15,** 2228–2237.

——, J. Paret, and P. Tabeling, 1999: Richardson pair dispersion in two-dimensional turbulence. *Phys. Rev. Lett.,* **82,** 2872–2875.

Kellay, H., and W. I. Goldburg, 2002: Two-dimensional turbulence: A review of some recent experiments. *Rep. Prog. Phys.,* **65,** 845–893.

Kennedy, A. B., 2005: Fluctuating circulation forced by unsteady multidirectional breaking waves. *J. Fluid Mech.,* **538,** 189–198.

——, Q. Chen, J. T. Kirby, and R. A. Dalrymple, 2000: Boussinesq modeling of wave transformation, breaking, and runup. I: 1D. *J. Waterway Port Coastal Ocean Eng.,* **126,** 39–47.

Kraichnan, R. H., 1966: Dispersion of particle pairs in homogeneous turbulence. *Phys. Fluids,* **9,** 1937–1943.

Kuik, A. J., G. P. van Vledder, and L. H. Holthuijsen, 1988: A method for the routine analysis of pitch-and-roll buoy wave data. *J. Phys. Oceanogr.,* **18,** 1020–1034.

Lewin, J., 1979: Blooms of surf-zone diatoms along the coast of the Olympic Peninsula, Washington. X. Chemical composition of the surf diatom *Chaetoceros armatum* and its major herbivore, the Pacific razor clam *Siliqua patula. Mar. Biol.,* **51,** 259–265.

Lin, J.-T., 1972: Relative dispersion in the enstrophy-cascading inertial range of homogeneous two-dimensional turbulence. *J. Atmos. Sci.,* **29,** 394–396.

MacMahan, J. H., A. J. H. M. Reniers, E. B. Thornton, and T. P. Stanton, 2004: Surf zone eddies coupled with rip current morphology. *J. Geophys. Res.,* **109,** C07004, doi:10.1029/2003JC002083.

Nwogu, O., 1993: Alternative form of Boussinesq equations for nearshore wave propagation. *J. Waterway Port Coastal Ocean Eng.,* **119,** 618–638.

Obukhov, A. M., 1941a: Spectral energy distribution in a turbulent flow. *Dokl. Akad. Nauk SSSR,* **32,** 22–24.

——, 1941b: Spectral energy distribution in a turbulent flow. *Izv. Akad. Nauk SSSR,* **5,** 453–466.

Okubo, A., 1971: Oceanic diffusion diagrams. *Deep-Sea Res.,* **18,** 789–802.

Oltman-Shay, J., P. A. Howd, and W. A. Birkemeier, 1989: Shear instabilities of the mean longshore current. 2. Field observations. *J. Geophys. Res.,* **94,** 18 031–18 042.

Peregrine, D., 1998: Surf zone currents. *Theor. Comput. Fluid Dyn.,* **10,** 295–309.

Raubenheimer, B., R. T. Guza, and S. Elgar, 1996: Wave transformation across the inner surf zone. *J. Geophys. Res.,* **101,** 25 589–25 597.

Reeves, R. L., S. B. Grant, R. D. Mrse, C. M. C. Oancea, B. F. Sanders, and A. B. Boehm, 2004: Scaling and management of fecal indicator bacteria in runoff from a coastal urban watershed in Southern California. *Environ. Sci. Technol.,* **38,** 2637–2648.

Reniers, A. J. H. M., J. H. MacMahan, E. B. Thornton, and T. P. Stanton, 2007: Modeling of very low frequency motions during RIPEX. *J. Geophys. Res.,* **112,** C07013, doi:10.1029/2005JC003122.

Richardson, L. F., 1926: Atmospheric diffusion shown on a distance-neighbour graph. *Proc. Roy. Soc. London,* **110A,** 709–737.

Romer, G., and A. McLachlan, 1986: Mullet grazing on surf diatom accumulations. *J. Fish Biol.,* **28,** 93–104.

Ruessink, B. G., J. R. Miles, F. Feddersen, R. T. Guza, and S. Elgar, 2001: Modeling the alongshore current on barred beaches. *J. Geophys. Res.,* **106,** 22 451–22 463.

Schiff, K. C., M. J. Allen, E. Y. Zeng, and S. M. Bay, 2000: Southern California. *Mar. Pollut. Bull.,* **41,** 76–93.

Schmidt, W. E., B. T. Woodward, K. S. Millikan, R. T. Guza, B. Raubenheimer, and S. Elgar, 2003: A GPS-tracked surf zone drifter. *J. Atmos. Oceanic Technol.,* **20,** 1069–1075.

Spydell, M., F. Feddersen, R. T. Guza, and W. E. Schmidt, 2007: Observing surf-zone dispersion with drifters. *J. Phys. Oceanogr.,* **37,** 2920–2939.

Stommel, H., 1949: Horizontal diffusion due to oceanic turbulence. *J. Mar. Res.,* **8,** 199–225.

Talbot, M., and G. Bate, 1987: Rip current characteristics and their role in the exchange of water and surf diatoms between the surf zone and nearshore. *Estuarine Coastal Shelf Sci.,* **25,** 707–727.

Taylor, G. I., 1921: Diffusion by continuous movements. *Proc. London Math. Soc.,* **20,** 196–212.

Wei, G., J. T. Kirby, S. T. Grilli, and R. Subramanya, 1995: A fully nonlinear Boussinesq model for surface waves. I. Highly nonlinear unsteady waves. *J. Fluid Mech.,* **294,** 71–92.

——, ——, and A. Sinha, 1999: Generation of waves in Boussinesq models using a source function method. *Coastal Eng.,* **36,** 271–299.